
# NEUTRON DETECTION USING AMORPHOUS BORON-CARBIDE HETERO-JUNCTION DIODES

THESIS

Thomas P. McQuary, Major, USA

AFIT/NUCL/ENP/12-M06

**DEPARTMENT OF THE AIR FORCE**
**AIR UNIVERSITY**

***AIR FORCE INSTITUTE OF TECHNOLOGY***

**Wright-Patterson Air Force Base, Ohio**

AFIT/NUCL/ENP/12-M06

# NEUTRON DETECTION USING AMORPHOUS BORON-CARBIDE HETERO-JUNCTION DIODES

THESIS

Presented to the Faculty

Department of Engineering Physics

Graduate School of Engineering and Management

Air Force Institute of Technology

Air University

Air Education and Training Command

in Partial Fulfillment of the Requirements for the

Degree of Master of Science

Thomas P. McQuary, BS

Major, USA

March 2012

AFIT/NUCL/ENP/12-M06

# NEUTRON DETECTION USING AMORPHOUS BORON-CARBIDE HETERO-JUNCTION DIODES

Thomas P. McQuary, BS
Major, USA

Approved:

| | |
|---|---|
| LTC John W. McClory (Chairman) | 11 MAR 12 Date |
| James C. Petrosky, PhD(Member) | 07 Mar 12 Date |
| LTC Stephen R. McHale (Member) | 07 MAR 12 Date |

AFIT/NUCL/ENP/12-M06

# Abstract

The high energy products of the $^{10}B(n,\alpha)^{7}Li$ neutron capture reaction were explored as a means of thermal neutron detection in thin film amorphous boron carbide (a–$B_5C$:$H_x$) on n-type silicon hetero-junction diodes. The diodes were produced via plasma-enhanced chemical vapor deposition. A second, resistive type device exploiting the same reaction products to detect neutrons was also tested. Pulse height spectroscopy was conducted on the diodes while they were subjected to a moderated plutonium-beryllium (PuBe) source with a thermal neutron flux of 464 [n/cm$^2$–s].

Neutron capture could not be confirmed experimentally in any of the devices tested. Cadmium shielding was used to discriminate between neutron-induced signals and other interactions. Both diodes failed to produce a pulse height spectrum with identifiable features, either with or without cadmium. The activity observed from the resistive device was conclusively determined to not be a result of a neutron interaction. The cadmium wrap produced pulses with a greater frequency and amplitude than previously observed in the unshielded spectra, and the observed signal was attributed to photon down-scattering in the cadmium shield.

Device modeling was performed to investigate the cause for the diode detector's negative response. A simulated 1.47 MeV $\alpha$ particle produced transient current of $10^{-7}$ A and the induced charge was 4.7 times less than intrinsic noise charge of the preamplifier. Further investigation of the model emphasized the transient current magnitude was most dependent on the electric field strength. The possibility of direct-conversion hetero-junction neutron detectors was not experimentally confirmed in this study. Proof-of-principle simulations using only 10 $\mu$m of silicon however did generate transient currents 2 factors larger than steady-state reverse bias currents.

# Table of Contents

Page

# List of Figures

Figure Page

Figure Page

# List of Tables

# List of Abbreviations

# List of Symbols

| Symbol | | Page |
|---|---|---|
| $\sigma$ | microscopic cross section | 8 |
| b | barn | 8 |
| eV | electron volt | 8 |
| $k$ | Boltzman constant | 8 |
| $T$ | Temperature | 8 |
| K | Kelvin | 8 |
| ns | nanoseconds | 13 |
| nA | nano-amperes | 14 |
| $\mu_p$ | hole mobility | 23 |
| $\mu_n$ | electron mobility | 23 |
| $N_T$ | Total Carrier Density | 23 |
| $E_g$ | band gap energy | 23 |
| mm | milimeter | 29 |
| $J$ | current density | 32 |
| $n_i$ | intrinsic carrier density | 33 |
| $J_s$ | saturation current density | 34 |
| $\eta$ | ideality factor | 34 |
| $C_j$ | Junction Capacitance | 37 |
| $A$ | Diode area | 37 |
| $\epsilon_s$ | Semiconductor permittivity | 37 |
| $W$ | Depletion width | 37 |
| $x_n$ | depletion width into the silicon | 40 |

Symbol Page

NEUTRON DETECTION USING AMORPHOUS BORON-CARBIDE HETERO-JUNCTION DIODES

# I. Introduction

## 1.1 Background

Through the end of the Cold War in 1991, the stockpiles of special nuclear material (SNM) were tightly controlled by the world's most powerful states. Special nuclear material as defined by Title I of the Atomic Energy Act of 1954 includes Pu, $^{233}$U, and uranium enriched in the isotopes $^{233}$U or $^{235}$U [1]. The fall of the Soviet Union precipitated a lapse in the security of SNM with profound effects, and the threat of proliferation of SNM has been a global concern ever since.

Several nations have gained possession of SNM since 1991. Some of these states, especially the Republic of North Korea and Iran, have adversarial stances with the United States. Nuclear states with unstable governments pose considerable risks to the United States, and to some degree, the rest of the world. Extremist organizations have demonstrated their desire to inflict harm on the US and its allies; they are limited only by their means to acquire the tools to do so. The 2001 terrorist attacks against the United States removed all doubt of this, and for the foreseeable future, changed the American sense of security and made the threat of SNM proliferation a relevant concern.

Detection at standoff distances of a minimum of several meters is an inherent requirement for intercepting any attempt to smuggle SNM into the US through regular points of entry, especially in shipping ports where large containers help to cover up

any nuclear signature. Detecting SNM presents an additional challenge for standoff detection. Most isotopes of SNM, $^{240}$Pu being the only exception, does not have significant spontaneous fission neutron emission rates. $^{240}$Pu has a spontaneous fission neutron emission rate of ˜920 [n/g–s] [2]. Furthermore, gamma ray emission for typical SNM isotopes with nontrivial emission rates is mostly below 200 keV for decays [3]. The limited range for gamma-rays and neutrons makes it very easy to shield highly enriched uranium (HEU) and weapons grade plutonium (WGPu).

Cosmic-ray induced spallation neutrons further complicate matters since, when generated at high Z/air interfaces, can cause a neutron background of ˜0.077 [n/cm$^2$–s]. Typical background for air/sea interfaces is less (around 0.012 [n/cm$^2$–s]). A hypothetical weapons mass of 4 kg of 94% $^{239}$Pu WGPu is detectable in an environment where high Z/air interfaces abound. This hypothetical mass of WGPu has an isotropic neutron flux on the order of 0.39 [n/cm$^2$–s] at a distance of 3 m assuming no shielding or moderation [4]. A hypothetical mass of HEU (25 kg for an implosion-type weapon) on the other hand emits neutrons at a rate four orders of magnitude less than WGPu, resulting in a neutron flux well below background levels at 3 m. If there was significant gamma shielding but no neutron specific shielding, it is feasible that WGPu could be detected from its neutron emission signature while HEU would go undetected due to its weak neutron emission activity.

The method of SNM detection described in this thesis is based solely on neutron counting rates above background levels. Gamma and X-ray spectrometers detect the ionizations caused by those photons interacting within the active detector volume. The amount of ionization created by a particle is dependent on its kinetic energy and the energy required to create charges within the material through which it is passing. Neutrons do not cause ionizations directly and as result, a real-time neutron spectrometer has not yet been realized [5]. The false-positive and false-negative report

rates can therefore improve only by more accurate and reliable neutron counting-rate based systems.

An effort to integrate neutron-sensitive material into solid-state devices dates back more than twenty years. Solid-state detectors offer several ways of improving neutron detector capabilities in areas where other detector types cannot. Scintillation detectors have relatively poor energy resolution and slow timing characteristics. Charge collection in proportional counters is limited due to the great differences in the electron and ion mobilities in the gas. Ion mobilities can be orders of magnitude less than electron mobilities, and as a result, the time constant of detection circuits will only allow for electrons to contribute to the output signal. Furthermore, some isotopes important in proportional counters designed to detect neutrons, namely $^{3}$He, are limited in supply and consequentially, there is additional emphasis placed on finding alternative neutron detection solutions. Semiconductors on the other hand, offer superior energy resolution, fast timing characteristics, and are relatively compact. The main issue challenging their use as neutron detectors stems from the fact that most popular semiconductor materials have low sensitivity to neutrons.

The primary consideration for a detector is the interaction rate between the detector medium and the incident radiation. This rate is driven by the cross section and density. Semiconducting boron carbide has a large thermal neutron capture cross section as shown in Figure 1. Second only to $^{157}$Gd (considering only isotopes that can form semiconducting solids), the large $^{10}$B thermal neutron capture cross section improves the probability of inducing a neutron interaction. Boron carbide is also a dense material (~2.5 [g cm$^{-3}$]). The combined effect of these two qualities increases the neutron interaction rates, and reduces the neutron mean free paths in the detector. The mean free path is of critical importance when developing compact detectors in the sense that the active volume of the detector should be large enough to stop a

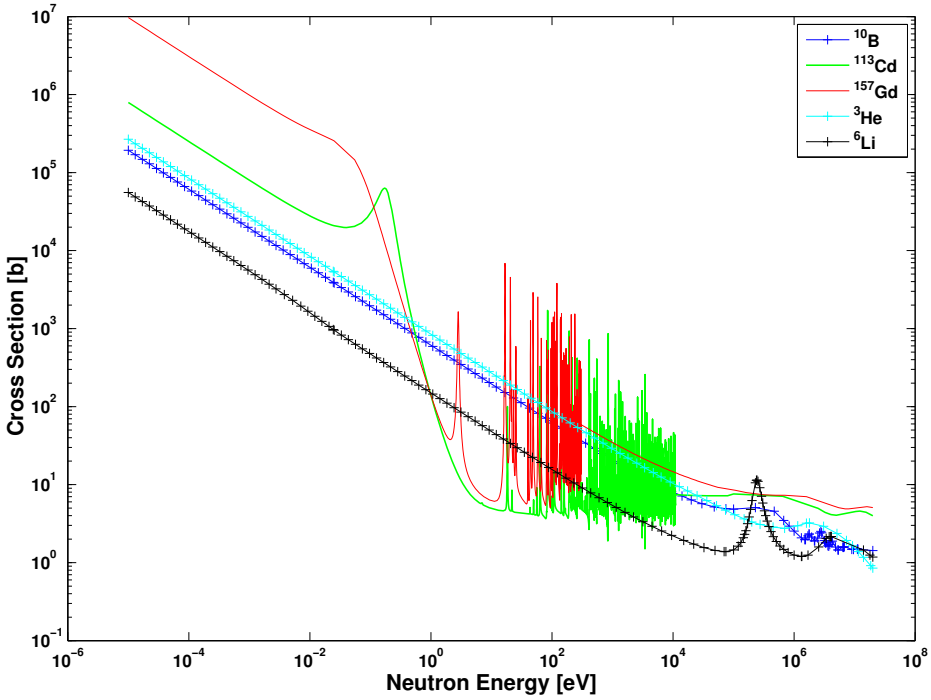


**Figure 1. Total neutron cross section of isotopes common to neutron detection [6].**

majority of the particles incident upon it.

$^{10}$B captures thermal neutrons and emits $^{7}$Li and $^{4}$He particles according to (1). It is of no use to have a high probability of capturing neutrons and produce reaction products that are still difficult to detect. This is clearly not the case with boron; the capture products are highly energetic and can can deposit all of their energy in only a few microns.

$$^{10}\mathrm{B} + \mathrm{n} \longrightarrow \begin{cases} 94\% & ^{4}\mathrm{He}(1.47\ \mathrm{MeV}) + ^{7}\mathrm{Li}(0.84\ \mathrm{MeV}) + \gamma(0.48\ \mathrm{MeV}) \\ 6\% & ^{4}\mathrm{He}(1.78\ \mathrm{MeV}) + ^{7}\mathrm{Li}(1.02\ \mathrm{MeV}) \end{cases} \tag{1}$$

Furthermore, boron has a low Z-number and is not highly sensitive to gamma radiation. Figure 2 shows that boron has significantly smaller cross sections in comparison with other semiconducting elements used in radiation detection. For these reasons, semiconducting boron carbide has been pursued for more than fifty years [8]. However,

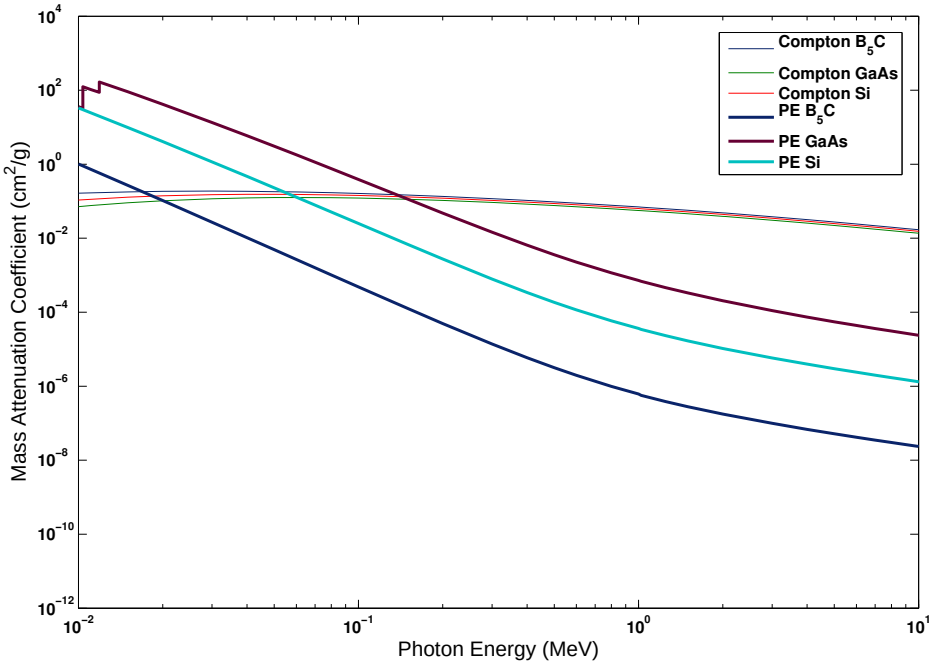


**Figure 2. Photoelectric and Compton Scatter mass attenuation coefficients for semiconducting compounds used for neutron detections [7].**

it is only recently that material science and technology capabilities have advanced far enough to consider the employment of boron carbide in neutron detectors.

## 1.2 Research Objectives

Boron carbide devices have been used in the past to detect neutrons. Most of these experiments were performed with boron carbide films deposited adjacent to the active region of a detector (conversion-layer devices are discussed in Section 2.1.2) [9, 10, 11, 12, 13]. Because the intrinsic efficiency of these detectors, roughly 4% [14], is low compared to other detection methods, variations in geometry and fabrication techniques have been explored relentlessly.

The diodes used in this study were constructed with amorphous boron carbide films deposited on high resistivity n-type silicon wafers. The objective in doing so was to create neutron-sensitive hetero-junction diodes where neutron capture byprod-

ucts were created within the active detection region. Due to the complications and challenges involved with amorphous/crystalline hetero-junction fabrication, articles claiming to have successfully detected neutrons with direct-conversion hetero-junction diodes are few in number. In fact, most articles pertaining to this specific subject are simulations-based [9].

The objective of this study was to detect thermal neutrons using amorphous-boron-carbide-on-silicon hetero-junction diodes. In order to correctly assess the detectors' performances, the diode material and semiconducting properties were meticulously studied. The ultimate failure of the diodes to detect neutrons was closely linked to these properties, as well as geometric parameters. Negative experimental results usually lead to follow-on experiments to determine the root cause of failure. In the case of this study, the causes for unsuccessful neutron detection were pursued through computer simulation and modeling. Taurus Davinci was used to model the device and the electrical transport of injected charges. This simulation confirmed post-characterization *ab initio* calculations predicting that depletion widths were adequate to completely stop the injected charge, but the weak electric fields and hence, the slow drift velocities, were identified as the root cause for poor charge collection efficiency.

# II. Theory

Neutron detection capabilities have lagged behind detectors of other radiations such as gamma or alpha particles. This is primarily due to the lack of an efficient solid-state neutron detector [9]. While still in early stages of development, solid-state neutron detectors have been constructed from a variety of elements capable of being incorporated into semiconducting solids and possessing high neutron cross sections. Most of the successful diodes thus far have been conversion layer devices (Section 2.1.2). This research investigates the use of boron carbide/silicon hetero-junction diodes to detect thermal neutrons. The experimental approach of this study stems from fundamental neutron detection principles, coupled with the physics of solid-state detectors. This chapter contains a brief review of neutron detection and a discussion of boron carbide and its properties that make it suitable and appealing for neutron detection.

## 2.1 Neutron Detection

Neutrons carry no electronic charge, and therefore cannot be detected directly using the measurement of electronic current or potential. Some neutral particles, such as gammas, interact with materials in ways that cause ionizations, and the resulting electrons can then be collected and measured. Neutrons do not cause ionizations directly but may result in nuclear reactions. Some nuclear reactions generate products that can ionize atoms within the detector volume, and this premise is the basis for the detectors used in this research. Not all neutron interactions are useful in detection however.

Once a neutron interacts with a target nucleus, one of two processes may occur. The first possibility is an elastic collision. This situation may change the neutron

energy and/or direction, but likely will not prompt the production of charged particles. In contrast, an atom can absorb, or capture, the incoming neutron and emit secondary radiations in the form of heavy charged particles. There is a finite and energy-dependent probability of either type of interaction to occur.

This probability, referred to as the cross section per nucleus, $\sigma$, is measured in units of barns (1 b = $10^{-24}$ $cm^2$). Neutrons of a fixed energy have a constant probability for each nuclear reaction mechanism (such as elastic scattering or capture reactions). Because the cross section may vary up to several orders of magnitude depending on the neutron energy, detector designs and methods differ greatly for neutron detection in different energy regions. It is conventional to refer to neutrons with respect to their kinetic energy. Neutrons having kinetic energies below the *cadmium cutoff* (or 0.5 eV) are designated as "slow neutrons". "Fast neutrons", or neutrons whose kinetic energies exceed 0.5 eV, can be detected with equipment and procedures different from those used for slow neutron detection. Detection of fast neutrons is not the focus of this work, and thus will only be periodically mentioned.

Slow neutrons scatter elastically with an atom, or experience one of several neutron capture reactions. Elastic scattering occurs when slow neutrons collide with target nuclei in the absorbing media but have insufficient kinetic energy to transfer a large amount of energy to that nucleus. Elastic collisions serve an important role in neutron detection by acting as a moderating force for the neutrons. This force reduces neutron kinetic energy into thermal equilibrium with the media. Thermal energy is on the order of $kT$ where $k$ is the Boltzman constant ($8.62\times10^{-5}$ eV/K), $T$ is temperature, and correlates to 0.0258 eV at room temperature (˜300 K).

### 2.1.1 Detector Properties

Thermal neutron detectors use materials with constituents that have high cross sections for thermal neutron capture reactions. Some of the more common isotopes incorporated into thermal neutron detectors are shown in Figure 1 [6]. Naturally occurring elements may actually be composed of two or more isotopes. For neutron detector materials and elements, one of the isotopes must have a high thermal neutron capture cross section in order to reliably lead to nuclear reactions; the remaining isotopes in the material may have very low cross sections and the detector's successful operation is unaffected by their presence. Figure 1 shows the total cross section for specific isotopes as opposed to the cumulative cross section calculated by the ratios of isotopic abundance in naturally occurring elements. The isotope pertinent to neutron detection must be of high abundance, or an economical method of enrichment must exist in order for the material to be a viable means of detecting neutrons.

In addition to having large thermal neutron capture cross sections, reactions employed for slow neutron detection preferably result in heavy charged particles [14]. This is the case with some of the isotopes referenced in Figure 1; they all have a high probability to capture neutrons and as indicated by (2 – 6), these reactions all have have large *Q-values* as well. The Q-value is the amount of energy released by a reaction. Reactions with large Q-values may deposit a greater amount of energy within the detector volume.

$$^{10}_{5}\mathrm{B} + ^{1}_{0}\mathrm{n} \xrightarrow{3840\text{ b}} ^{4}_{2}\alpha + ^{10}_{5}\mathrm{Li} + \gamma + 2.31\text{ MeV or }2.79\text{ MeV} \quad (2)$$

$$^{3}_{2}\mathrm{He} + ^{1}_{0}\mathrm{n} \xrightarrow{5330\text{ b}} ^{3}_{1}\mathrm{H} + ^{1}_{1}\mathrm{H} + 764\text{ keV} \quad (3)$$

$$^{113}_{48}\mathrm{Cd} + ^{1}_{0}\mathrm{n} \xrightarrow{21000\text{ b}} ^{114}_{48}\mathrm{Cd} + \gamma + 9.042\text{ MeV} \quad (4)$$

$$^{6}_{3}\mathrm{Li} + ^{1}_{0}\mathrm{n} \xrightarrow{940\text{ b}} ^{3}_{1}\mathrm{H} + ^{4}_{2}\alpha + 4.78\text{ MeV} \quad (5)$$

$$^{157}_{64}\mathrm{Gd} + ^{1}_{0}\mathrm{n} \xrightarrow{255000\text{ b}} ^{158}_{64}\mathrm{Gd} + \gamma + \mathrm{IC}_{-1}^{0}\mathrm{e} + 7.937\text{ MeV} \quad (6)$$

Neutron reactive films based on the $^{157}$Gd(n,$\gamma$)$^{158}$Gd reaction have higher probabilities than $^{10}$B(n,$\alpha$)$^{7}$Li, or $^{6}$Li(n,$\alpha$)$^{3}$H based films of capturing neutrons for a fixed film thickness because of the high $^{157}$Gd thermal neutron cross section. However, the combined emission of low energy gamma rays, the small branching ration of internal conversion electrons, and the long range of the internal conversion electrons make neutron-induced events easily hidden by background gamma-ray events. This is because only a small number of those internal conversion electrons will generate sufficient charge to exceed the intrinsic noise level of commercial charge-sensitive preamplifiers. The particle energies emitted from the $^{6}$Li(n,$\alpha$)$^{3}$H reaction are greater than those emitted from the $^{10}$B reaction. Yet, the optimized film thickness for $^{6}$LiF is over ten times greater than needed for $^{10}$B with relatively unimproved neutron detection efficiency due to the lower cross section for capture [12].

It is also common to use cadmium foils as a means of discriminating between those signals induced by neutrons versus the signals caused by other radiation sources. As will be discussed later, this approach was used during this research as a means of positively identifying neutron signals.

One final consideration for a detector is its sensitivity to gamma radiation. Gammas are ubiquitous to most neutron-rich environments and therefore must be accounted for. As shown in (2), (4), and (6), gammas can be a product of the reaction ultimately responsible for the generating a signal. Gamma rays can ionize and excite atoms within the detector; both cases result in unwanted detector output which can ultimately complicate the task of detecting neutrons. Neutron detectors should therefore be constructed of material with low gamma sensitivity, but must also have a geometry that will also prevent large-scale gamma interference. For example, most neutron proportional counter tubes are smaller in diameter than the mean free path of most gamma rays. Gammas can then pass through the detector and deposit only

a portion, if any, of their energy.

### 2.1.2 Detector Technologies

Radiation detectors typically fall into one of three classes: proportional counters, scintillators, and solid-state detectors. Although the term solid-state is somewhat ambiguous since scintillation detectors could technically be considered solids, the accepted practice is to categorize only those detectors whose signal is based on the collection of electron-hole pairs as solid-state detectors. More simply stated, solid-state devices are almost always semiconducting detectors, and for this reason, both terms will be used interchangeably throughout this document.

The purpose of this research is to improve existing methods for detecting neutrons. An understanding of earlier methods used in neutron detection work will help gauge the success of current research efforts, and to what degree. Therefore, this section contains of brief overview of non-solid state neutron detectors in addition to a more in-depth explanation of this work's central theme, semiconductor properties and detectors.

#### 2.1.2.1 Non-solid-state detectors

Proportional counters used in neutron detection are commonly cylindrical tubes filled with $^3$He or $BF_3$ gas. Figure 3 depicts the basic proportional counter configuration. An electric field is established in the detector by applying high voltage to the anode. When exposed to thermal neutrons, charged particles created by (2) or (3) ionize gas molecules in the detector, resulting in electron drift towards the anode. Strong electric fields can generate a cascade of ionizations when electrons gain sufficient kinetic energy to cause ionizations when they collide with gas molecules. The secondary electrons are accelerated by the electric field. This gas multiplication

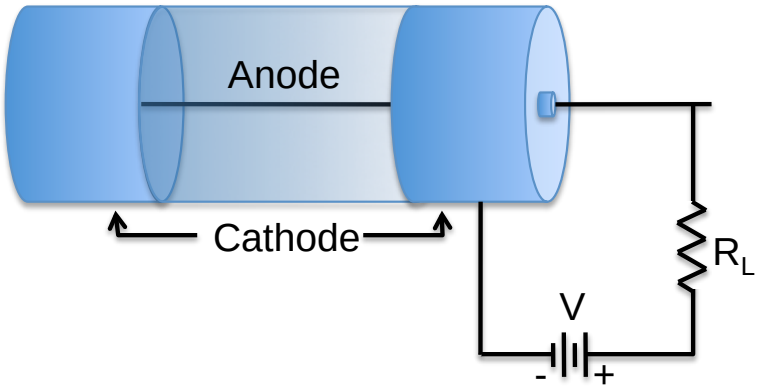


**Figure 3. Basic elements of a proportional counter. The cathode ensures there is a vacuum-tight enclosure to contain the fill gas. Positive voltage is applied to the anode wire which creates an electric field perpendicular to the longitudinal axis (z-axis) [14].**

process is known as the *Townsend avalanche*.

Scintillators are commonly used in fast neutron detection, but also can be used in slow neutron detection with inorganic lithium-containing crystals. The crystal lattice in the scintillator determines the energy states of the material. Although electrons are typically found in the valence band, neutron absorptions can excite electrons into the conduction band. The products of the $^{6}$Li(n,T)$^{4}$He reaction (5) deposit 4.78 MeV to the crystal lattice. Photons are emitted by the process of fluorescence when the electrons relax from the conduction band to the valence band. Photo-multiplier tubes are commonly incorporated into scintillator detectors in order to collect photons and convert them via photo-sensitive layers into photoelectrons which can then be multiplied in order to yield a measurable current pulse. Although beyond the scope of this research, scintillators are commonly used in fast neutron detection as well. This form of detection relies on the recoil protons produced when high-energy neutrons collide elastically with atoms in the scintillator lattice.

#### 2.1.2.2 Solid-state detectors

Solid-state, or semiconductor, detectors rely on the formation of electron-hole pairs, analogous to electron-ion pairs in gas-filled proportional counters, to generate a signal. Ionizing radiation interacts with solid matter in the detector and deposits energy, elevating valence band electrons to the the conduction band. Physically, this simply represents an electron gaining sufficient energy to leave the bonding site and drift, under an electric field, through the crystal lattice [14]. This process creates a vacancy, or hole, in the valence band. The amount of energy required to create an electron-hole pair, or the ionization energy, is dependent on the band gap of the semiconductor. Temperature is another factor in the semiconductor ionization energy, but to a much smaller degree. With an applied electric field, both the electrons in the conduction band (holes in the valence band) will respond to electrostatic forces and result in a net migration of charge.

The motion of both electrons and holes will be a combination of both diffusion and drift velocity [14]. The motion of electrons will be anti-parallel to the electric field, but the drift velocity of holes is conceptually more difficult to grasp. The hole represents the absence of a negative charge, thereby creating a net positive charge. Both electron and hole drift velocities are proportional to the electric field at low to medium field strengths. With sufficiently large electric fields, the saturation velocity is reached. Section 3.3.1 will examine this topic more closely, but charge collection time corresponds to the time required for the charges to transport from the point of generation to the depletion region boundary. Most detectors are operated at saturation so that the charged particles will be accelerated from the depletion region with the greatest possible velocity, thereby minimizing the charge collection times (ideally on the order of a ns).

Electron or hole movement constitutes a current that persists until the charge

carrier reaches the boundary of the detector's active volume. Assuming energy is deposited at a single point, the resulting carrier currents will still be different because the charge collection times vary with the carrier mobilities. In some modern semiconductor detectors, hole mobilities are close enough to electron mobilities such that both carrier currents can be integrated on a measuring circuit with a long time constant. This is not feasible in proportional counters where the ion mobility is orders of magnitude greater than the electron mobility [14].

Solid-state detectors emphasized in this work are based on the properties near a junction of *n*- and *p*- type semiconducting material. The effects of carrier diffusion across this *p-n junction* gives rise to an electric field and a region depleted of majority charge carriers, the depletion region. The premise of diode radiation detectors is that the electron-hole pairs created within the depletion region are swiftly accelerated out of the region by the electric field. The motion of the charges produces an output current pulse. This transient current is measurable only if the steady state leakage current is sufficiently low. Ideally, the leakage currents should be on the order of a nA, or $10^{-9}$ A [14]. The pulse rise time is defined by migration time from the point of formation to the boundary of the depletion width.

In the absence of an applied voltage, the natural built-in voltage across the depletion width causes the carriers to drift, but the performance of the detector will be inherently poor under these circumstances. This is due to the higher probability for recombination and charge trapping when the carriers move slowly through the depletion region, an event the depletes the charge collection potential.

The fraction of charges escaping capture increases as the electric field becomes stronger. Reverse biasing the diode increases the the electric field and the thickness of the depletion region [15]. This depletion region represents the active volume of the detector. As will be discussed in Section 3.3.2, devices used in this study were only

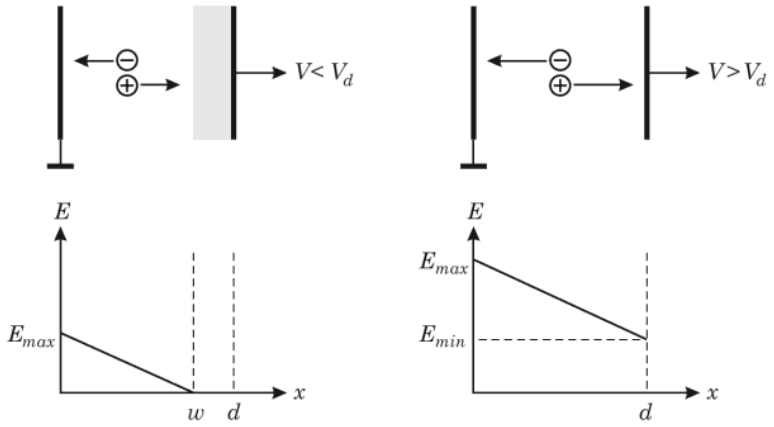


**Figure 4. Electric field comparison between fully- and partially-depleted detectors [16]**

partially depleted. Most detectors are operated fully-depleted for several reasons. Figure 4 effectively illustrates the differences in the electric fields for detectors that are partially depleted (shown on the left) versus those that are fully depleted (shown on the right). In the figure, $w$ signifies the edge of the depletion boundary and corresponds to the distance from the junction where the electric field vanishes, which has deleterious effects on the drift velocity, pulse rise time, and the increases the probability of charge trapping. The un-depleted *dead layer* between the depletion region and the electrode is also source of noise and can deteriorate the detector resolution.

In fully-depleted detectors, the electric field exists throughout the diode as a whole because depletion region spans the whole width between the two electrodes. As the applied bias increases, the electric field increases, and the difference between $E_{max}$ and $E_{min}$ is minimized. Eventually, if the bias continues to increase, the electric field will become uniform throughout the diode [16].

**Solid-state thermal neutron detectors.** Solid-state thermal neutron detectors incorporate material with high cross sections for neutron capture interactions. Conversion layers and solid-state direct conversion devices (Figure 5) both employ

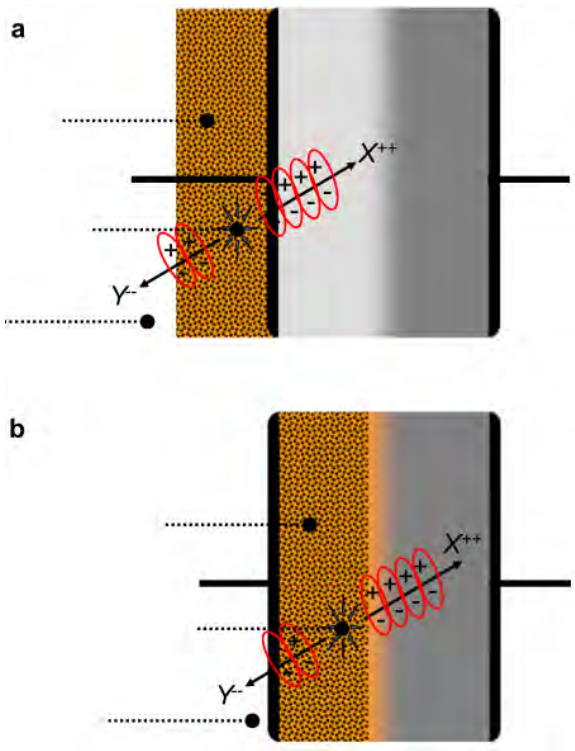


**Figure 5. Comparison of (a) conversion layer and (b) direct conversion diodes [5].**

neutron induced reactions. The most common reactions used to produce detectable ionization are the $^{10}$B(n,$\alpha$)$^{7}$Li, $^{6}$Li(n,$\alpha$)$^{3}$H, and the $^{113}$Cd(n,$\gamma$)$^{114}$Cd reactions [12].

Planar conversion layer devices use neutron-sensitive thin-films deposited adjacent to a diode under reverse bias. Reaction products emitted close enough to and in the direction of the diode junction can create electron-hole pair production within the depletion region of the reverse-biased diode. The electric field present in the detector minimizes the recombination of the electron-hole pairs. As the thin-film thickness increases, so does the probability of capturing a neutron and producing charged particles. These reaction products travel finite distances in material prior to depositing all of their energy. Thin-films that are too thick may absorb all of the charged particle energy before the particle reaches the detector volume. An additional factor concerning conversion layer devices is the inherent cap in intrinsic efficiency.

The incoming thermal neutron energy (0.0259 eV) is quite low compared to the Q-value of the reaction. Both resultant products are emitted in opposite directions in order to conserve momentum. Thus, there is a high likelihood that only one reaction product will be emitted in the direction of the detector volume.

Direct conversion, or *solid-form* [12], devices overcome the disadvantages characterizing conversion layer devices by integrating the neutron-sensitive thin film within the diode junction. In semiconductor detectors, the measurable signal originates from electron-hole pair formation in the depletion region. The obvious advantage to solid form devices is that the neutron interaction occurs within the active detector region and all reaction products are capable of producing detectable ionizations. Factors such as the film thickness, the location and direction of the emitted particles, bias voltages, recombination rates, and the material properties of the film itself all determine the probability of producing a measurable signal.

## 2.2 Properties of Boron Carbide

Few elements possess a neutron capture cross section suitable for neutron detectors. Even fewer elements meet this criteria and are also capable of forming semiconducting solids. Boron accomplishes both criteria. $^{10}$B is 20% abundant in naturally occurring boron and has a large capture cross section for thermal neutrons. Boron also forms a boron-rich semiconducting solid, boron carbide [17], which exists in many forms. Most of the literature addressing the semiconducting properties of boron carbide focus on the crystalline form with B:C ratios ranging from 4.3:1 to 11:1 [18, 19, 20, 21, 22, 23]. The boron carbide incorporated into the devices used in this study were amorphous, which is the least well referenced form of boron carbide. This gap in knowledge precludes direct comparisons between devices cited in the literature and the devices used in this study without taking into account how the amorphous

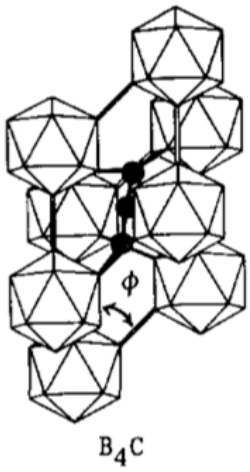


**Figure 6. Typical rhombohedral lattice structure in semiconducting boron carbide [24].**

structure affects the physical properties.

While amorphous structures lack a recurrent long-range order, the semiconductor properties of the material do not appear to depend upon crystallite size [8]. Similarities between crystalline and amorphous boron carbide, as will be reported in Section 2.2.1, will be basis of the following discussion. The significance of the similarities leads to a logical conclusion: The principles associated with crystalline boron carbide, such as crystal structure and electrical transport phenomena, are also closely related to the principles of the amorphous counterpart.

### 2.2.1 Structure

Crystalline BC structures vary but are often icosahedral-crystal type structures with rhombohedran lattice structures as shown in Figure 6. The crystal structures of boron carbides, including amorphous structures, share the icosahedron building block that is also found in rhombohedral boron [25]. The icosahedral is the primary conduction mechanism for the material. The presence of two carbon atoms, serving as electron donors, slightly distorts the molecular polyhedral cage structure [26]. Figure 7 shows the molecular structure of ortho- and meta-carborane

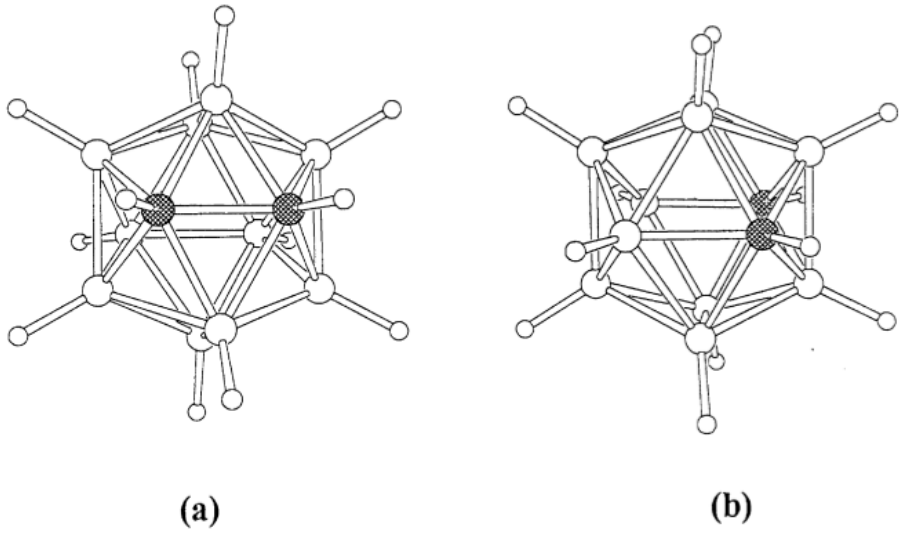


**Figure 7. Molecular structure of (a) ortho- and (b) meta-carborane $C_2B_{10}H_{12}$. Carbon atoms are shaded [26].**

atoms. When either molecule is used as a chemical vapor deposition precursor, the chiral differences between the isomers lead to different majority-carrier semiconductors. Meta- carborane (closo-1,7-dicarbadodecaborane) forms an n-type semiconductor while ortho-carborane (closo-1,2-dicarbadodecaborane) forms a slightly p-type semiconductor [27]. Ortho-carborane deposited by Plasma-Enhanced Chemical Vapor Deposition (PECVD), forms an amorphous semiconductor denoted as a–$B_5C$:$H_x$. A schematic picture of this structure is shown in Figure 8.

The semiconducting properties of boron carbide make it uniquely suitable for detection diodes. Semiconducting films can be incorporated in a p-n junction, thereby removing the requirement for a neutron sensitive conversion layer adjacent to the diode [5, 9]. Furthermore, the consequence of forming different majority-carrier semiconductors can be exploited to create an all-boron carbide heteroisomeric diode. Meta-carborane/ortho-carborane used as deposition precursors in sequence have produced rectifying diodes [29].

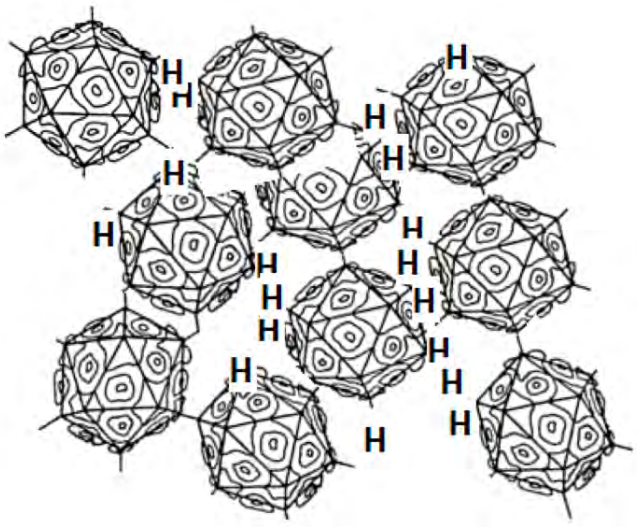

**Figure 8. Schematic depiction of a–$B_5C$:$H_x$ [28].**

### 2.2.2 Boron Carbide Electrical Transport

Boron carbide forms micro-crystalline structures, and no unit cell describes the structure as a whole [18]. The electrical transport properties of boron carbide are not well understood, but one theory, from the works of Werheit *et.al.*., is the current dominant theory. Preceding Werheits theory is an explanation based on a model proposed by Emin *et.al.* [30]. From his works, Emin argues that bipolaron hopping is responsible for boron carbide electrical activity. Recent experimental evidence published by Werheit *et.al.* contradict the theory and provide findings incompatible with the presence of bipolarons in boron carbide [19, 21, 22, 23].

Werheits model contends the semiconducting nature is derivative from the high density of anti-site and vacancy defects [20]. The theory follows from theoretical band structure calculations and the proposed band diagram is shown in Figure 9 [23]. Point defects in semiconductors generate split-off valence states in the band gap. These unoccupied valence states, according to calculated electron deficiencies and experimentally determined point defect densities, are exactly compensated in real solids. This implies both that the material is a semiconducting solid and the valence bands

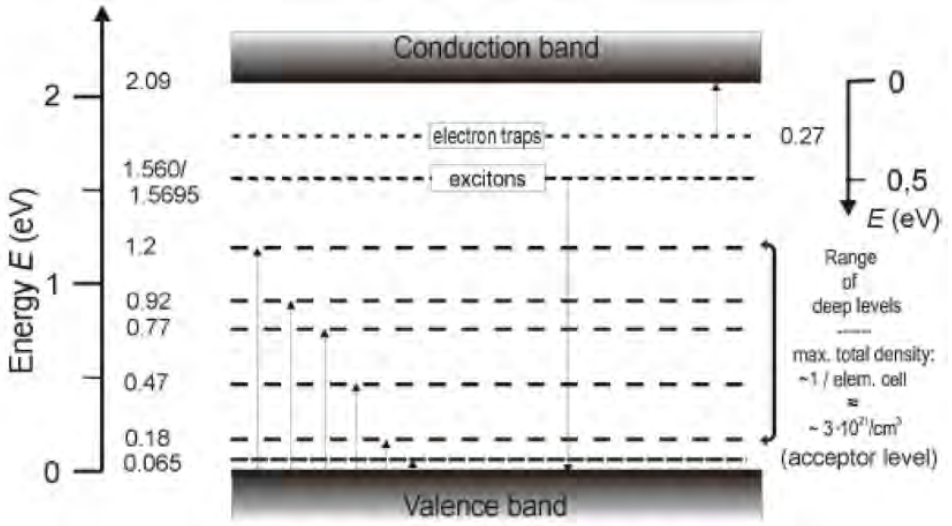


**Figure 9. Energy band scheme based on optical absorption, luminescence, XRS, and transport properties. Left ordinate, energies related to the valence band edge; right ordinate, energies relative to the conduction band edge. Arrows indicate the direction of the measured optical transition [23].**

are completely filled. The electron deficiency evokes the generation of compensating intrinsic defects, likely for energetic reasons. Such high concentrations of gap states attached to the valence band affect the electronic charge transport; essentially, they are responsible for the p-type character and the very low electrical conductivity [18].

Dowben *et.al.* [31] have attempted to determine the band gap of boron carbide via optical absorption measurements at varying ratios of boron to carbon (Figure 10). The results indicate the band gap is closely correlated with the boron to carbon ratio and can range from 0.77 to 1.80 eV and is consistent with the thermal activation barrier of 1.25 eV for conductivity [31]. This conclusion differs from the 2.09 eV band gap of Figure 9. Any direct comparison between the reports however is possibly flawed. First, it is possible the 0.9 eV band gap indicated by the optical absorption measurements is a non-direct transition between the gap states and conduction band. No attempt is made in [31] to clarify whether the reported values reference non-direct transitions or indirect transitions from the valence to the conduction band. Several

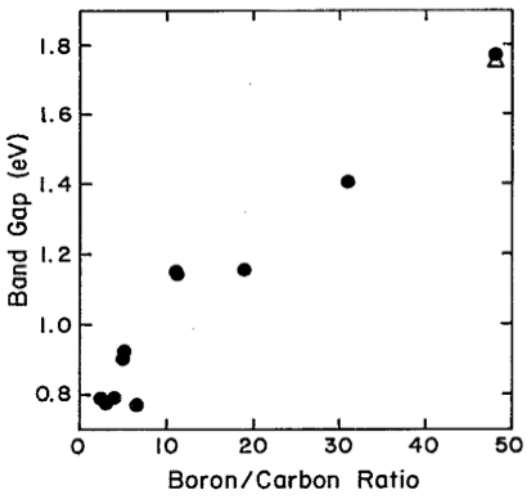


**Figure 10. Band gaps determined (for a–$B_5C$:$H_x$) at room temperature are plotted against composition determined by Auger electron spectroscopy. The measurement are largely determined by optical absorption • but data for photoluminescence △ is also shown [31].**

non-direct transitions determined through optical absorption in polycrystalline boron carbide, including one 0.92 eV transition, are mentioned in [23].

High electron deficiency induced gap states results in high carrier concentration on the order of $10^{18}$ – $10^{19}$ as shown in Figure 11(a) [20]. Drude-type transport coupled with a hole hopping mechanism within the partially filled gap states is responsible for transporting charge carriers through the boron carbide [21].

The large number of gap states increases the probability of trapping. As shown in Figure 11(b), Werheit reports boron carbide ambient mobilities converging to values on the order of 1 [$cm^2$/V–s] [20].

However, charge collection measurement times typical of p-type a–$B_5C$:$H_x$ thin films on n-type silicon diodes exposed to a neutron field result in calculated mobilities on the order of $10^{-2}$ – $10^{-4}$ [$cm^2$/V–s] [17]. The reduced mobility in thin films is likely due to greater defect site concentrations expected of amorphous solids versus poly- or mono-crystalline solids. Table 1 summarizes some of the electronic properties discussed herein.

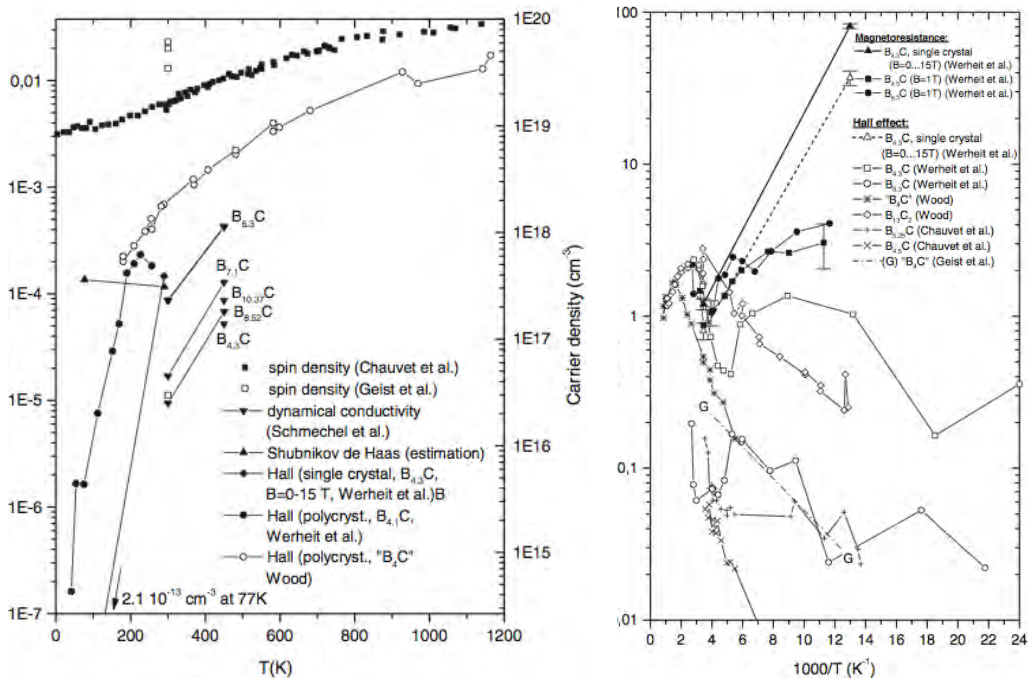


**Figure 11. (a) Comparison of carrier densities and (b) Carrier mobility in boron carbide as reported by different experimental methods and authors [20].**

## 2.3 Previous Work

Boron carbide has been shown to form excellent hetero-, and hetero-isomeric junctions that have stable leakage currents close to ideal levels [32]. Some of the neutron detection studies performed in the past give great insight in how to conduct the current research, as well as interpret and analyze data.

**Table 1. Electronic properties of boron carbide**

| Parameter | Symbol | Value | |
|---|---|---|---|
| | | Werheit | Dowben |
| Mobility | $\mu_p$ | 1 $cm^2$/V–s [18] | $10^{-2}$ – $10^{-4}$ $cm^2$/V–s [17] |
| | $\mu_n$ | | 0.001 $cm^2$/V–s [17] |
| Total Carrier Density | $N_T$ | $10^{18}$ – $10^{19}$ $cm^{-3}$ [18] | |
| Dopant Concentration | $N_A$ | | $4.5\times10^{12}$ $cm^{-3}$ [17] |
| Band gap energy | $E_g$ | 2.09 eV [23] | 0.77 – 1.88 eV [31] |

**Conversion-layer devices.** Conversion-layer devices were among the first approaches to implement semiconductor devices for neutron detection. The neutron capture products are only produced in the the neutron-sensitive film; for the purposes of this discussion the film is boron carbide. As the film thickness increases, the probability of capturing incident neutrons increases and approaches unity with sufficiently thick conversion-layer thickness. In other words, the capture efficiency is theoretically 100%.

While the neutron capture efficiency improves with the thicker films, a point is reached where the overall detector efficiency suffers as result of excessive film thicknesses. The $^{7}$Li and $^{4}$He particles deposit energy immediately from the point of generation. All of the energy deposited by the charged particles in the boron carbide region will be lost due to recombination. If the particles deposit all of their energy by this manner, they are said to have "self absorbed." Thus, it is possible to capture thermal neutrons with great efficiency but still have none of the resulting energy deposited in the detector.

In contrast, particles born within a infinitesimally thin film will likely deposit only a small fraction of their energy before reaching the detector. These competing factors pose a difficult dilemma in determining the best detector design using conversion-layer films. McGregor *et.al.* have explored this problem in great detail with numerical models and boron carbide conversion-layer device simulations and as result, have reported optimized parameters regarding the specific geometry of devices.

Figure 12(a) and 12(b) summarize their findings. Figure 12(a) shows that the least energetic particle, $^{7}$Li at 840 keV, deposits all of its energy in less than 2 $\mu$m. In comparison, the predominant $\alpha$ particle of the reaction will deposit 870 keV (1470 keV – 600 keV) over the same distance [11]. Figure 12(b) represents the optimized parameters that factor in to the overall detector efficiency. Due to the differ-

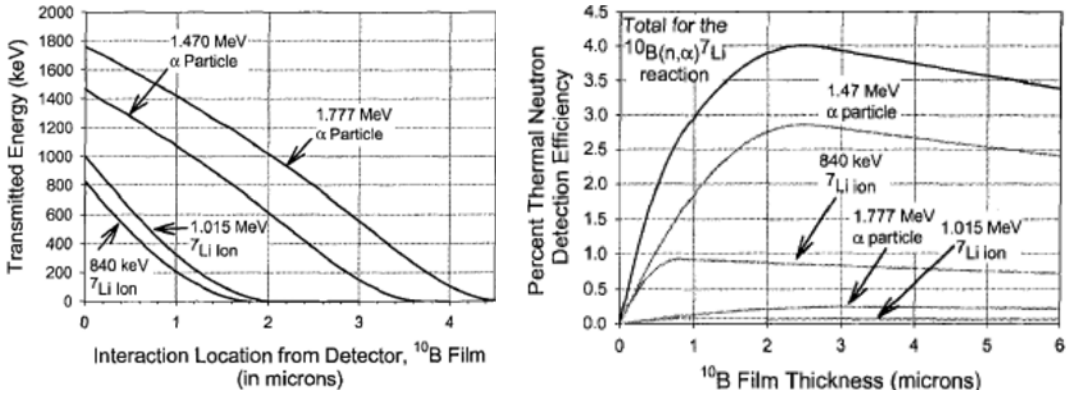


(a) (b)

**Figure 12. (a)$^{7}$Li and $^{4}$He range (in boron carbide) and, (b) film thickness optimization determined from a computational analysis [11].**

ences in track length shown in Figure 12(a), the optimum film thickness varies with respect to each of the four particles [11]. With that said however, it is safe to conclude that the intrinsic efficiency suffers with films greater than 2.5 $\mu$m.

The pulse-height spectra taken from conversion-layer diodes typically exhibit two or more spectral features. A perfect example of this is presented in Figure 13 [33]. Both reaction products are emitted back to back, and only one, if either, forms electron-hole pairs within the detector. The two dominant peaks correspond to $^{7}$Li and $^{4}$He at 840 keV and 1.47 MeV. The 1.02 MeV $^{7}$Li is likely masked within the continuum of the $^{4}$He peak at 1.47 MeV.

**Direct conversion devices.** The feature most notable regarding conversion-type devices is the absence of a full-energy peak, or a peak corresponding to the total Q-value of the reaction. Most of the work done thus far dealing with direct-conversion diodes has been computer model-based. In fact, many authors claiming to have successfully detected neutrons via direct-conversion devices have incorrectly analyzed pulse-height spectra data by failing to note the absence of the full energy peak [12]. Figure 14 [9] shows that the the diode geometries play a significant role in the detec-

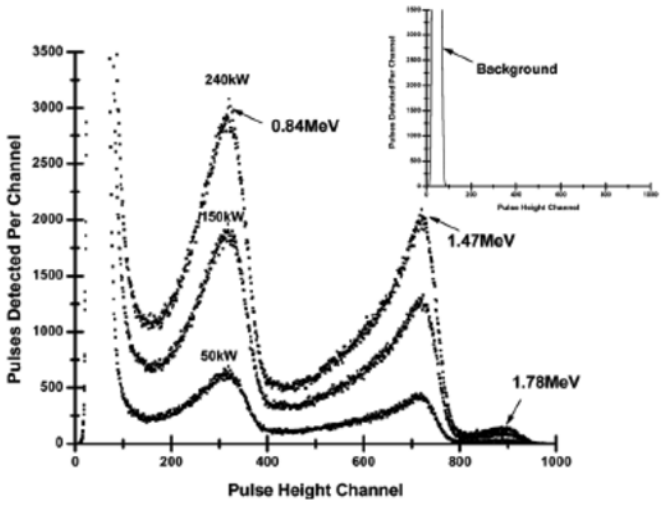


**Figure 13. Pulse height spectra collected using conversion-layer diode [33].**

tor response to neutrons. Immediately, one notices two significant differences. First, both spectra exhibit a continua around the Li and He peaks, but the conversion layer signatures have tailing towards lower energies and direct-conversion devices have tails that extend towards higher energies. In conversion layer devices, the particles deposit energy before reaching the detector volume, and the particle generation site, direction, and path length all contribute to an energy continuum below the full energy value of the particle. A similar effect is observed in direct conversion devices. This is explained by the following argument. Whenever charged particles are created, one particle will likely deposit only some of its energy while the other makes a full energy deposition. The energy from both particles is collected simultaneously, but path length of the particle will create a continuum as well. In this case however, the energy is integrated with the energy of the oppositely directed particle.

Secondly, the direct-conversion device shows two full escape peaks for both reaction possibilities. These peaks cannot occur in conversion devices. As the film thicknesses grow larger, the spectra tend to flatten at lower energies, and the two full energy peaks grow in count number. In other words, the thickness of the film is

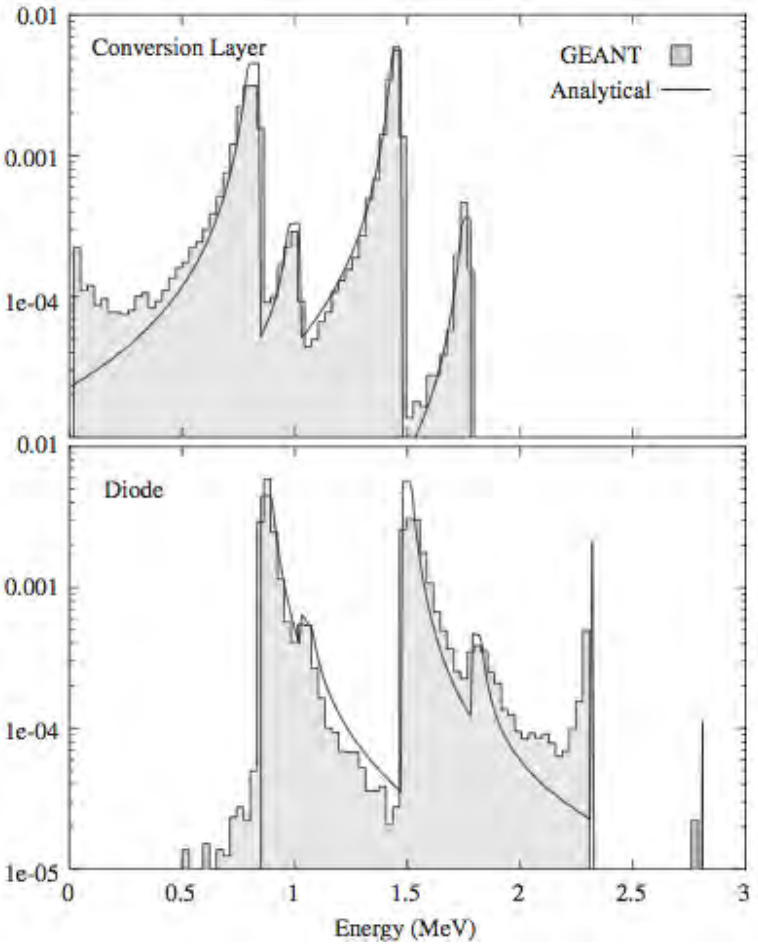


**Figure 14. Computer simulation prediction of both a conversion-layer and direct conversion diode spectra [9].**

sufficiently thick to stop both particles within the active detector volume.

# III. Experimental Approach

## 3.1 Device Fabrication

This study was performed using three different devices. Two of devices were hetero-junction diodes. One diode was fabricated at the University of Missouri, Kansas City (UMKC). The second diode was fabricated in 2010 at the University of Nebraska, Lincoln (UNL). It is worth noting that UNL diode was used in conjunction with thesis work in 2010. A resistive type device was the second class of device tested during this research; it was also constructed at UNL. The underlying physics and materials science involving the fabrication processes for these devices is beyond the scope of this thesis, but a brief description of the fabrication process is included. This chapter comments briefly on the fabrication procedures for the devices used in this research (a more detailed procedure can be obtained from [34, 35]), and followed by the device precharacterization and experimental procedures.

### 3.1.1 Hetero-junction Device

**UMKC Diode.** The diodes were prepared in a custom-built capacitively coupled PECVD reactor by the reaction of ortho-carborane vapor in a 200 mTorr argon background. The use of PECVD provides the means for fabricating boron carbide thin films at lower temperatures and pressures (<1000 °C, <50 Torr) [31]. The boron carbide is assumed to have a much greater carrier concentration than the high resistivity silicon. The dopant concentration, $N_D$, for 10 [k$\Omega$–cm] n-type silicon is on the order of $10^{11}$ cm$^{-3}$ [15]. The function of high resistivity (low dopant concentration) silicon is two-fold. The overall space charge neutrality must be maintained (the total space charge on either side of the junction is equal), and is given by (7). $x_p$ and $x_n$ correspond to the depletion thickness on the p- and n-side of the junction, respectively.

The greater carrier concentration on the boron carbide side, $N_A$, will deplete a greater volume on the high purity silicon side.

$$N_A x_p = N_D x_n \tag{7}$$

Dopants can also act as traps within the active detector volume. Thus, high purity silicon results in greater depletion widths for relatively thin boron carbide films. Charge carriers produced as a result of energetic charged particles will be less likely to become captured by traps within the active detector volume.

High resistivity (>10 [k$\Omega$–cm]) n-type silicon (111) wafers with a thickness of 515$\pm$20 $\mu$m were used for the substrate. The wafers were diced into square pieces of 15$\times$15 mm for film deposition and device fabrication purposes. Before the vapor deposition process could be performed, the substrates were cleaned using a Piranha solution to remove the organic impurities from the surface and were chemically etched in hydrofluoric acid to remove surface oxides. The cleaned substrates were rinsed with acidified deoxygenated water and dried using IPA vapor. This five-step sequence ensured organic impurities, particulates and surface oxides were minimized.

Once cleaned and dried, the substrates were inserted into a carousel cradle assembly, capable of holding nine substrates. The assembly rotated during deposition for film uniformity. Care was taken to ensure all nine substrates were loaded into the plate assembly and transferred to the primary PECVD reactor chamber within 15 minutes to prevent new oxides from developing on the clean surfaces. The cradle assembly formed the positive electrode in the PECVD system and was powered by RF generator operating at 13.56 MHz. Using a custom solid-source bubbler, solid ortho-carborane precursor was sublimed at 72 – 75 °C and delivered to the reactor with an argon carrier gas. The gaseous argon/carborane mixture was released into the reactor chamber through a shower head, which also formed the negative electrode

to the capacitively coupled PECVD system [34].

Once the boron carbide films were grown, elipsometric measurements were performed to determine the film thickness. The film had a thickness of 1.5±0.2 $\mu$m. A secondary sputtering chamber was used to deposit aluminum contacts on the diode. The contacts on the boron carbide side were deposited using a 0.2 $cm^2$ shadow mask. The boron carbide-Al layer was protected using photoresist and the reverse side of the substrate was cleaned using hydrofluoric acid solution, and was rinsed and dried using the procedure above. This was done to ensure the surface oxides had been removed prior to contact deposition. The photoresist was removed by dipping the device in acetone solution after the contacts were deposited on the reverse side.

The device, now having aluminum contacts on both the boron carbide and silicon side, could be characterized and inspected for measured to determine if it functioned as a diode. It was first mounted on a fiberglass board with two separate copper-clad inlays (shown in Figure 15). The diode was affixed to the largest of the two copper-clad inlays. Conductive silver paint, lightly dabbed on the silicon (n-side) contact of the diode, served as both a means of connectivity between the n-side of the diode and the copper-clad contact, as well as a bonding agent to secure the diode in place. A thin copper wire connected the boron carbide (p-side) contact to the smaller copper inlay.

**UNL Diode.** Specifics regarding the geometry of UNL diode are estimated. The diode differs from UMKC diode in geometry, most notably in the boron carbide thickness and the contact composition and size. The diode was created via PECVD; a summarized discussion of this process can be found earlier in this section. Hemiseal was used to coat the device which prevented film thickness measurements. All other differences between UMKC and UNL diodes can be found in the Table 2. The UNL diode was secured to the fiberglass board in accordance with the procedure described

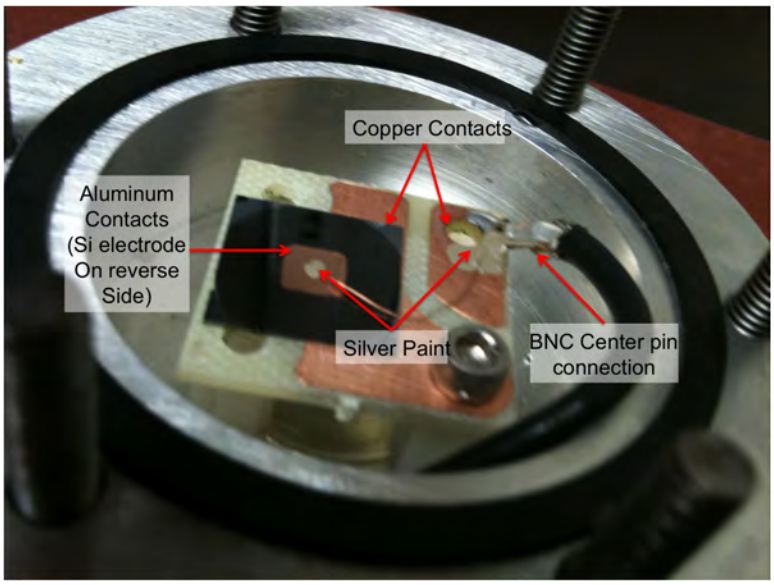


**Figure 15. Close-up photo of the diode. Aluminum contacts were sputtered onto both sides, and was mounted on fiberglass board. Silver paint secured the the n-side contact to the largest copper inlay. A thin copper wire connected the boron carbide (p-side) to the smaller copper inlay. The BNC center-pin wire is shown soldered to the p-side contact. The wire was detached and soldered to the n-side inlay for the neutron irradiation phase of this study.**

for UMKC diode.

**Table 2. Diode Material/Geometric Parameters**

| | UMKC Diode | UNL Diode |
|---|---|---|
| Silicon Resistivity | >10 [kΩ–cm] | 8 [kΩ–cm] [36] |
| Silicon Thickness | 515 [$\mu$m] | 525 [$\mu$m] |
| BC Resistivity | $10^8$ – $10^{10}$ [Ω–cm] [17] | $10^8$ – $10^{10}$ [Ω–cm] [17] |
| BC Thickness | 1.5 [$\mu$m] | 2.0 [$\mu$m] |
| Contact Area | $2.0\times10^{-1}$ [cm$^2$] | $3.32\times10^{-2}$ [cm$^2$] |
| Contact Metal | Aluminum | Silver chromate |

### 3.1.2 UNL Resistive-type Device

The UNL resistor-like device incorporates the neutron capturing potentials of $^{157}$Gd, $^{6}$Li, and $^{10}$B. Films of $Gd_2O_3$ and $Li_2B_4O_7$ were deposited on sapphire glass ($Al_2O_3$) via pulsed laser deposition (PLD) [35]. The gadolinium oxide film was limited

to 60 nm in order to avoid excessive gamma interference. $Li_2B_4O_7$ was deposited on the opposite side of the device. The PLD procedure was not a vital part of this study, the method of deposition is detailed in [35]. As with the diodes, a copper-clad fiberglass board was used to secure the device. Two $1.3\times10^{-2}$ $cm^2$ gold contacts on the gadolinium side of the film (facing away from the fiber-glass board) were successfully bound to the copper-clad firmly using conductive silver paint.

## 3.2 Pre-Irradiation Device Characterization

The Keithley 4200 semiconductor characterization system performed all prechar-acterization measurements during the course of this research via the the Signatone CM–220 probing station. All measurements were performed at approximately 300 K.

### 3.2.1 Diode I–V and C–V characterization

**I–V** The p-n junction serves as the rectifying element in the diode, allowing current to flow freely in one direction and inhibiting it in the other. Current-voltage (I–V) measurements were performed on both diodes to verify rectifying behavior and to characterize the diode leakage current. Due to the device area differences, a more useful comparison was the current density ($J$). In Figure 16, both diodes exhibit rectifying behavior. The y-axis (anode current density) is set on a logarithmic scale. The error bars are smaller than the pixel diameter of the plotted data. It is apparent that differences in time, fabrication location, and diode geometry affected the I–V characteristics, manifested by the differences in the current densities for all applied anode voltages. Figure 16 shows that the the forward and reverse bias currents densities differ by three orders of magnitude for the UMKC diode. The UNL diode rectification was considerably smaller with only two orders of magnitude difference between the forward and reverse bias currents.

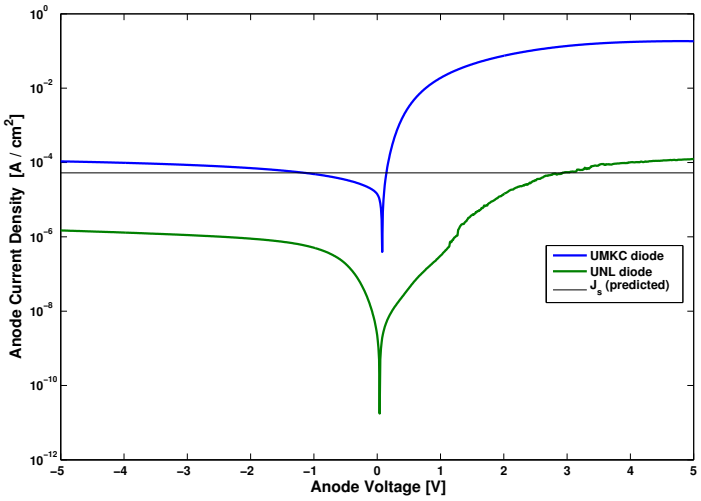


**Figure 16. J–V curve for UMKC(blue) and UNL(green) diodes (y-axis is a log scale). The predicted $J_s$ for the UMKC diode is plotted in black.**

Both diodes exhibited stable currents between 1.0 – 5.0 V reverse bias. The UNL diode produced a current density of $1.49(\pm 0.03)\times 10^{-6}$ and $1.24(\pm 0.03)\times 10^{-4}$ [A/cm$^2$] at 5.0 V reverse and forward bias respectively. The corresponding values for the UMKC diode are $1.07(\pm 0.06)\times 10^{-4}$ and $1.83(\pm 0.2)\times 10^{-1}$ [A/cm$^2$]. These values were compared to the the theoretical reverse saturation current density in order to quantify the leakage current.

Total diode current is given by the Shockley equation, also known as the ideal diode law (8). The equation, as written, was modified to account for different intrinsic carrier densities, $n_i$, of the different semiconductor materials involved in the hetero-structures [37]. $D$ and $L$ are the diffusion constants and lengths respectively for the minority carriers. $N_A$ and $N_D$ are the accepter and donor concentrations in boron carbide and silicon respectively. Under forward bias, the current density increases at a constant rate, and under reverse bias however, the current saturates at the reverse

saturation current.

$$J = \frac{D_n n_{i(bc)}^2 q}{L_n N_A} + \frac{D_p n_{i(si)}^2 q}{L_p N_D} \left[\exp\left(\frac{qV}{kT}\right) - 1\right]$$
$$= J_s \left[\exp\left(\frac{qV}{kT}\right) - 1\right] \tag{8}$$

Leakage current, caused by thermionic emission and carrier tunneling, has adverse effect on the signal-to-noise (S/N) ratio when using diodes as radiation detectors. In reference to Section 2.1.2, leakage currents on the order of nA are ideal. The saturation current density, $J_s$, was computed from values listed in Table 4 and is plotted in black in Figure 16. Appendix B.1.1 also contains this calculation. Some parameters determined experimentally did not agree with values reported in literature sources. Other parameters had large uncertainties due to the wide range of possible values. In these cases the mid-range value was used for the approximation (e.g. effective hole mass in boron carbide). Precise leakage current calculations could not be obtained for the UMKC diode due to these uncertainties. The leakage current was estimated to be $\approx$10 $\mu$A at -5 V, and calculated from (8) with the assumption that excess conductivity above the reverse saturation current was due to leakage.

When the experimental data are plotted against the Shockley equation (8), there is poor agreement between the measured values and the theoretical predictions of the forward current as shown in Figure 17(a). The ideal diode equation assumes an ideality factor ($\eta$) of 1.0. This is consistent with forward I–V characteristics when diffusion current dominants; $\eta$ increases as recombination current becomes dominant. A more accurate expression for diode current density is

$$J = J_s \left[\exp\left(\frac{qV}{\eta kT}\right) - 1\right]. \tag{9}$$

A least squares fit, shown in purple in Figure 17(b), of the linear forward current

corresponds to $\eta$=1.0 (the forward current is linear only with a semi-log scale). If we extrapolate the line towards the y-axis, the intercept occurs at the reverse saturation current density ($J(0V) = J_s$). The relatively weak correlation between the theory and experimental data is caused by a larger ideality factor for the UMKC diode. Using the the same y-intercept, a line tangent to the measured data was projected (shown in green in Figure 17(b)). The slope of the line corresponded to ideality factor of 3.5. The forward current sub-linearity prevented an effort to calculate the ideality factor empirically, or via the method described using the ideal diode forward current linear region. Shockley-Read-Hall recombination theory predicts an ideality factor equal to 2.0 or less. The deviation from this prediction is likely attributed to the high defect states of the amorphous boron carbide. The high defect density of boron carbide, on the order of $10^{21}$ $cm^{-3}$ [20], makes multi-level recombination possible. In the case of high defect densities, ideality factors can increase above Shockley-Read-Hall recombination predictions of $1.0 \leq \eta \leq 2.0$ [38].

Given the qualitative ideality factor analysis, it is not surprising that both diodes exhibited sub-linear forward current behavior. This is consistent with a high resistivity material. Boron carbide diodes characterized in [32] were compared to other hetero-junction diodes (ZnSe/ZnCdSe) and the sub-linearity of the forward current was interpreted as an effective resistor in series (both the amorphous boron carbide and n-type silicon have large impedences). The boron carbide films are highly resistive (on the order of $10^9$ $\Omega$–cm at room temperature), and the forward current-limiting behavior shown in Figure 16 can be attributed the diodes' highly resistive amorphous region [31, 32].

Due to the shortage of devices exhibiting proper rectifying I–V characteristics, break-down voltage analysis was omitted. A diode reverse biased to breakdown can show increases in leakage current. In diode detectors, depleting the diode to the

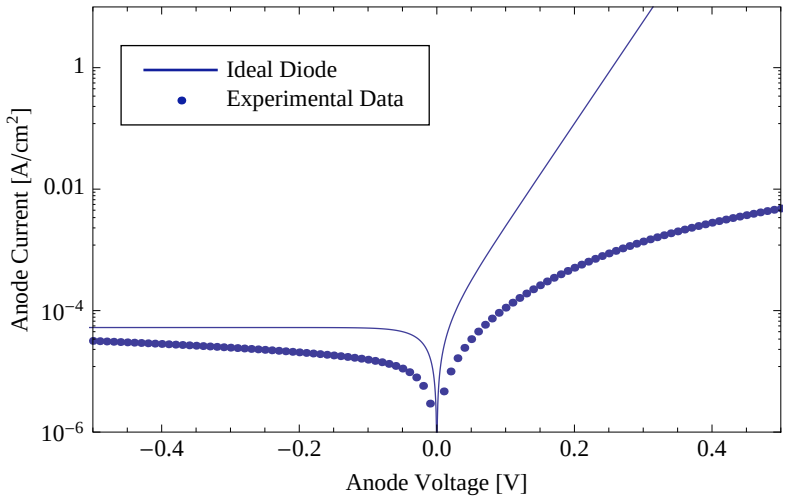


(a)

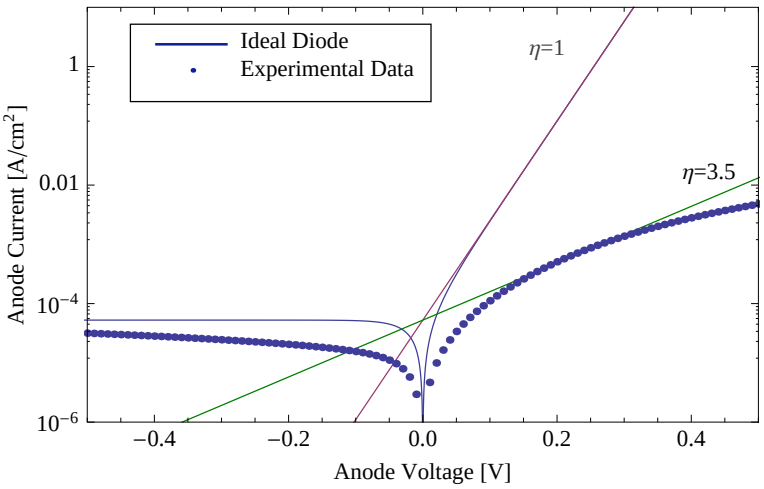


(b)

**Figure 17. (a) Current density of UMKC diode vs Shockley ideal hetero-structure model. (b) UMKC diode vs Shockley ideal model with linear region fits accounting for ideality factors.**

greatest possible extent is beneficial because it increases the active detector volume and improves charge collection efficiency. Determining the optimal detector bias may result in damaging diodes and given the limited number of samples available for testing during this study, breakdown analysis could not be performed.

**C–V** Under reverse bias, the diode junction acts like a parallel-plate capacitor. In order to calculate the depletion width of the diode, capacitance-voltage measurements (C–V), measurements were performed. Capacitance can be related to the depletion width of a diode via (10) where $C_j$ is the junction capacitance, $A$ is the diode area, $\epsilon_s$ is the semiconductor permittivity, and $W$ is the depletion width.

$$C_j = \frac{\epsilon_s A}{W} \tag{10}$$

The C–V measurements plotted in Figures 18(a) and 18(b) for each diode indicate the neither device's C–V characteristics are ideal. The left ordinate corresponds to the measured capacitance (converted to units of F $cm^{-2}$); the right ordinate corresponds to the inverse squared data ($1/C^2$). The UMKC diode capacitance exceeds the UNL diode capacitance by 1 – 2 orders of magnitude depending on the applied reverse voltage. Depletion inversely affects the junction capacitance (10), and the large UMKC diode capacitances indicate the diode is less depleted than than the UNL diode. Furthermore, achieving the smallest detector capacitance reduces electronic noise and can ultimately improve the detector resolution [14]. Thus, detectors are operated with the largest possible depletion region in order to maximize the radiation-sensitive volume, and to improve the S/N ratio by minimizing the capacitance.

Junction capacitance can be rewritten in terms of the semiconductor permittivities, dopant concentrations, and the applied voltage (11). The $1/\sqrt{V_{bi} - V}$ dependency corresponds to asymptotic increase in $C_j$ as the applied reverse bias approaches 0 V. It can also be inferred from (11) that junction capacitance does not exist when the forward bias exceeds $V_{bi}$. From this perspective, it is apparent the UNL diode has non diode-like C–V characteristics. In Figure 18(b), the capacitance increases as the reverse bias decreases (as expected). However, the peaking, followed by a decrease of the capacitance as the applied voltage approaches zero is indicative of some phenom-

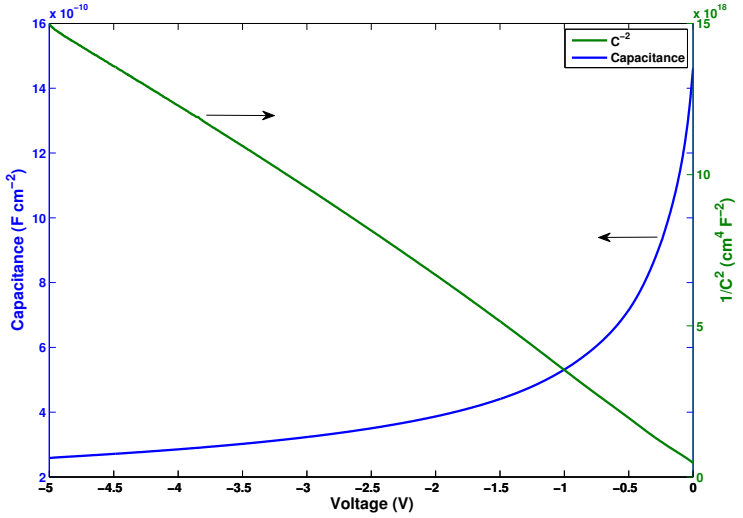


(a)

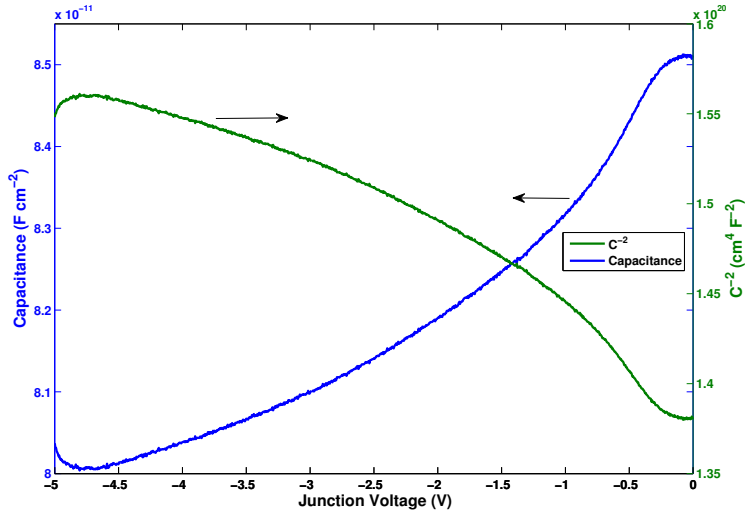


(b)

**Figure 18. Capacitance measurements for each diode. The left/right ordinate refers to the C–V/C$^{-2}$ measurement for (a) UMKC diode, and (b) UNL diode.**

ena other than junction depletion. Although the direct cause of this behavior was not investigated, it is possibly linked to radiation damage effects incurred from previous research.

$$C_j = \sqrt{\frac{q\epsilon_{si}\epsilon_{bc}N_D N_A}{2\left(\epsilon_{si}N_D + \epsilon_{bc}N_A\right)\left(V_{\text{bi}} - V\right)}} \tag{11}$$

Equation 11 can be manipulated algebraically so the function is linear with respect

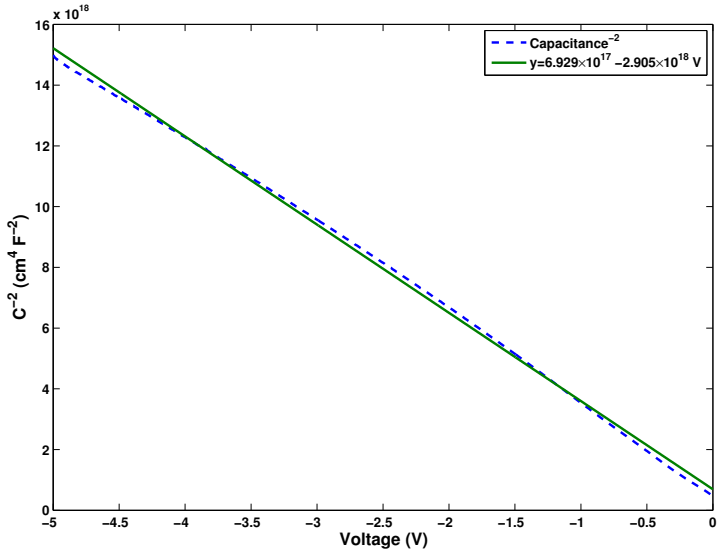


**Figure 19. $1/C_j{}^2$ of UMKC diode(blue) with linear fit (green).**

to the independent variable, $V$. The inverse-squared of (12) for an abrupt heterojunction diode results in a straight line. Figures 18(a) and 18(b) differ in this aspect. Only the UMKC diode $1/C_j{}^2$ plotted data is consistent with an abrupt junction; the corresponding UNL diode data produces a curved line which contradicts the abrupt junction assumption. The fabrication process for the UNL diode, discussed within [36], was the basis for this conclusion.

$$\left(\frac{1}{C_j}\right)^2 = \left(\frac{2\left(\epsilon_{si}N_D + \epsilon_{bc}N_A\right)\left(V_{\text{bi}} - V\right)}{q\epsilon_{si}\epsilon_{bc}N_D N_A}\right) \tag{12}$$

Figure 19 presents the UMKC diode $1/C_j{}^2$ data with a linear fit. The expression for this fit is included in the upper right corner of the figure. The correlation between the the two lines further supports that the junction is abrupt. A linear fit to the UNL diode $1/\text{Cj}^2$ data was not possible without excessive statistical uncertainty. $V_{bi}$ can be calculated from x-axis intercept of the fitted line. Using (12), when $V{=}V_{bi}$, $1/C_j{}^2{\equiv}\,0$. Appendix B.1.1 provides a detailed calculation for determining the UMKC

diode built-in voltage. Unfortunately, the lack of linearity exhibited by the UNL diode $1/C_j{}^2$ data precluded a similar fit for the built-in voltage. In order to estimate the individual depletion widths into the BC (where the doping density is not well known) and the silicon, the BC region was initially assumed to be fully depleted (a reasonable assumption based on [17]). The dopant concentration was much higher in the BC region than in the silicon [20], and the slope of the $1/C_j{}^2$ versus $V$ line was purely a result of depletion expanding in the silicon.

$$C_j = \left( \frac{\epsilon_n}{x_n} + \frac{\epsilon_p}{x_p} \right)^{-1} \tag{13}$$

$C_j$ for an abrupt hetero-junction is treated as the equivalent capacitance of a two-capacitor-in-series connection. The equivalent capacitance (13) was used to approximate the hetero-junction depletion width [39]. Using the measured capacitances (converted to F cm$^{-2}$), and the parameters listed in Table 3, the depletion width into the silicon, $x_n$, was calculated.

**Table 3. Variables used in depletion width calculation**

| Parameter | Symbol | Value |
|---|---|---|
| Permittivity of Free Space | $\epsilon_0$ | $8.85\times10^{-14}$ F cm$^{-1}$ |
| Silicon permittivity | $\epsilon_s$ | 11.9 $\epsilon_0$ |
| BC permittivity | $\epsilon_{bc}$ | 8.0 $\epsilon_0$ [40] |
| Junction capacitance | $C_j$ | (Measured) F cm$^{-2}$ |
| BC Thickness | $x_p$ | 1.5 (UMKC) $\mu$m<br>2.0 (UNL) $\mu$m |

Applying reverse bias to a diode widens the depletion width further into the silicon towards the n-side electrode, and increases the internal electric field within the depletion region. The detector efficiency benefits from both consequences of reverse bias. The result of the depletion width calculations is shown in Figures 20(a) and 20(b). Tables 4 and 5 summarize the calculations derived from the capacitance measurements for both diodes. The active detector volume predictions, the UMKC diode

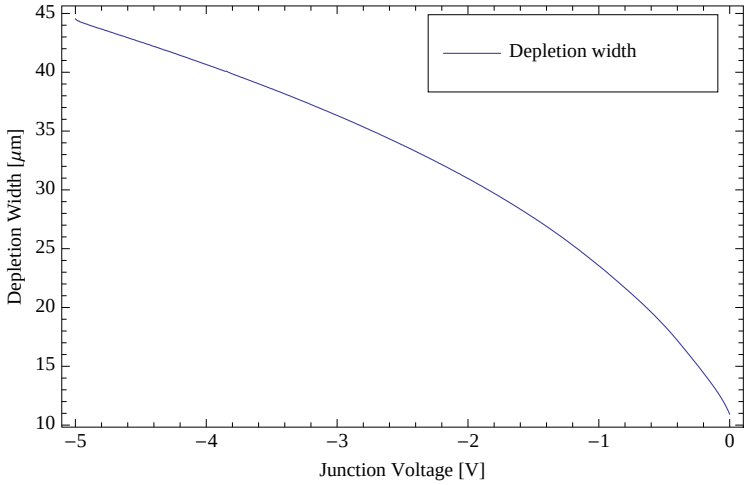


(a) UMKC diode depletion

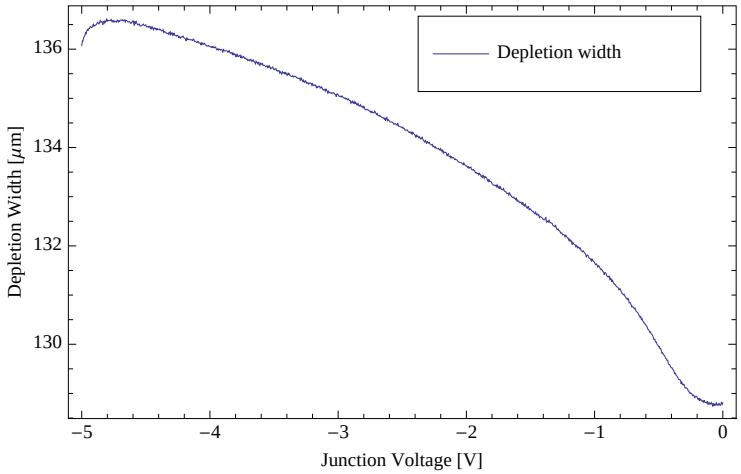


(b) UNL diode depletion

**Figure 20. Depletion width comparison under reverse bias.(a) UMKC. (b) UNL**

reverse saturation current density approximation, and the diode modeling during the final stages of this study were based on these values listed in the two tables. $N_A$ and $N_D$ were only calculated for the UMKC diode. The experimentally determined $N_D$ exceeded dopant concentrations expected for $\geq$10 [k$\Omega$–cm] n-type silicon as reported by [15] by 2 orders of magnitude. The boron carbide effective dopant concentrations reported by [17] coincided with the UMKC diode $N_D$ calculation within a factor of 1.6.

**Table 4. UMKC Diode Characterization Summary**

| Parameter | Value |
|---|---|
| $V_{bi}$ [V] | 0.23852 |
| $N_D$ [$cm^{-3}$] | $3.13\times10^{13}$ |
| $N_A$ [$cm^{-3}$] | $7.0\times10^{12}$ |
| $W_{0V}$ [$\mu$m] | 10.9402 |
| $W_{-5V}$ [$\mu$m] | 44.5261 |

**Table 5. UNL Diode Characterization Summary**

| Parameter | Value |
|---|---|
| $V_{bi}$ [V] | UNK |
| $N_{A,D}$ [$cm^{-3}$] | UNK |
| $W_{0V}$ [$\mu$m] | 128.804 |
| $W_{-5V}$ [$\mu$m] | 136.073 |

The depletion region volume is given by the product of the diode area and the depletion width. The active detector volumes are $8.9\times10^{-4}$ $cm^3$ and $4.5\times10^{-4}$ $cm^3$ for the UMKC and UNL diode respectively at 5 V reverse bias.

While the advantages of greater depletion width, namely a stronger electric field and greater detector volume, are clear, the device must be depleted sufficiently so that ionizing radiation can deposit most of its kinetic energy within the active detector volume. The $\alpha$ particles are the most energetic reaction products, and they will also have longest ionization track in both the boron carbide and silicon. The stopping power in silicon limits the track length to 6.0 microns. The depletion widths in both diodes exceed this length, and therefore, the detector is depleted adequately and will allow the charged particle products to deposit most, if not all, of their kinetic energies.

### 3.2.2 Resistor-like device characterization

The UNL resistive-detector was ultimately the only device to produce spectra with identifiable features. The I–V characteristics of the device, shown in Figure 21, are inconsistent to a degree with *Ohm's Law*, $V = IR$. In the case of a resistor,

the expected I–V dependency is linear. The data plotted in Figure 21 was collected by sweeping the voltage from -20 – 20 V. A slightly different curve resulted from a reverse sweep (higher to lower voltage).

The observed hysteresis vanished at -5 V, and as voltage was increased, the current gradually became linear with voltage. The inverse effect was observed for the high to low voltage sweep (not shown). In this case, hysteresis vanished at +5 V. Plotting both data sets together showed both linear regions were in fact parallel, with a slope coefficient that corresponded to $R^{-1}$. This demonstrated that the device was purely resistive, and for the purpose of clarity, only one of the sweeps was included in the figure to represent the I–V characteristics without needlessly convoluting the figure.

Based on the slope of the linear region, the resistance of the device is $8.93\times10^{10}$ Ω. An issue left unresolved is the slight conductivity at 0 V. This was partially due to charge trapping and surface transport [41]. The pre-characterization, performed using a probe station, was not performed in complete darkness. Aluminum oxide is a transparent material, and when exposed to light, could have also contributed to this

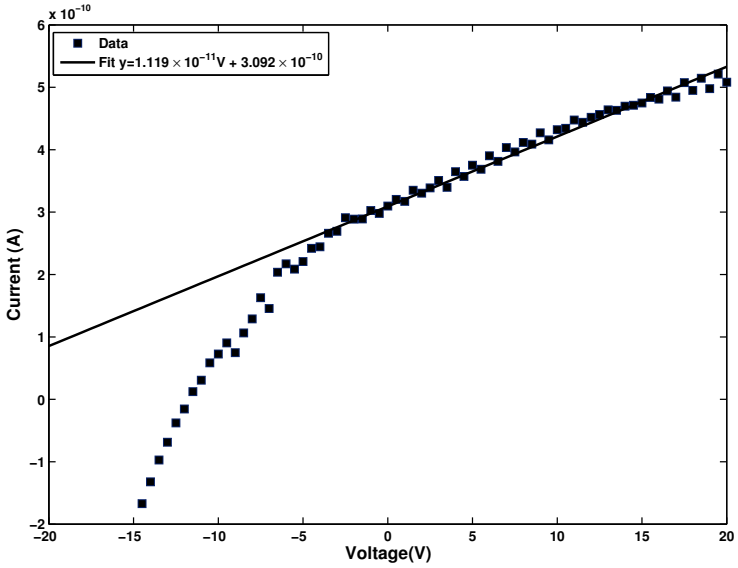


**Figure 21. I–V measurements resistor like device with linear fit of the I–V (linear region existed for $V_{applied}$ greater than -15 V).**

departure from the expected resistor characteristics.

## 3.3 Irradiation Experimental Procedure

The goal of the irradiation experiment was to determine if a hetero-junction diode constructed of a–$B_5C$:$H_x$ and n-type silicon could be used to detect thermal neutrons. Theory and modeling supports that the devices used for this study were properly configured to measure the products of the $^{10}B$ neutron capture reaction [5, 36]. These devices were fundamentally different from conversion type detectors and both of the reaction products ($^7Li$ and $\alpha$ particles) should have ionized carriers in the active detector region in spite of being emitted 180° from each other.

Many modifications were made until reaching the electrical connections and component configuration described below. Only the details pertinent to this final configuration are discussed. The over-arching concept behind the experiment was that any neutron-induced spectral feature observed in the unshielded pulse-height measurement would be suppressed with a cadmium foil. Cadmium is a highly efficient absorber of thermal neutrons (Figure 1), and with the device shielded with the foil, only energetic neutrons reach the detector. The boron carbide cross section was low for fast neutrons, and thus the probability of capturing the neutron was considerably less.

### 3.3.1 Electrical connections

The devices were packaged in an aluminum case as shown in Figure 22. The cases were constructed from 3-in diameter aluminum rods by creating a small central cavity inside to secure and protect the device during experiments. A small hole was drilled and tapped in the side in order to accept a threaded BNC connector. The purpose of this design was three-fold: it prevented damage to the device, muted electrical noise,


**Figure 22. Device mounted in aluminum case.**

and formed a large electrical ground. The BNC center coaxial pin was insulated from the aluminum case, but the ground (the outer metal wall of the connector) formed a direct (tension) contact with the case once it was securely tightened into the side-wall of the aluminum case. Four holes were drilled and tapped in the bottom of the case's internal cavity to match the spacings of the holes drilled through the fiberglass boards. The two holes drilled through corners with the copper-clad inlays served an additional purpose. The contact could be grounded to the case by tightening a steel bolt through the hole, which established a pressure contact between the copper inlay and the aluminum case (Figure 22). Nylon offsets screwed into the holes formed a mounting platform for the fiberglass boards. The nylon also functioned as an insulator and ensured no part of the board came in contact with the case.

Figure 23 depicts the electrical connections for the experiment. A small gauge

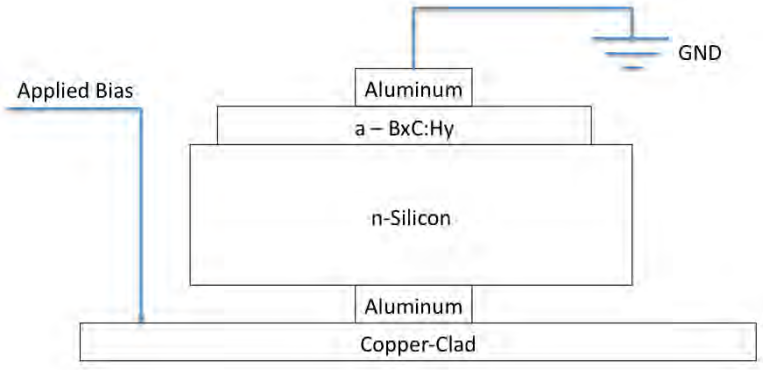


**Figure 23. Electronic connectivity setup.**

copper wire was used to connect the coaxial center-pin to the n-side copper contact. All spectral data was collected from the silicon (n-side) with the BC (p-side) grounded. Neutron capture occurred only in the p-side of the device; however, most of the charge was captured in the silicon [17]. Electron-hole pairs were created from the ionizing energy loss of the highly energetic $^{7}$Li and $^{4}$He particles and the predominant signal collected at the electrode was due to ionizations in the depletion region. Accordingly, electrons (holes) were accelerated towards the positive (negative) electrode.

Electron mobility, $\mu_n$ in silicon is 1350 [cm$^2$/V–s], whereas hole mobility in boron carbide is much less (approximately 0.00075 [cm$^2$/V–s]) [17]. The vast differences in carrier mobility also results in significant differences in the charge collection times. As the holes transport through the boron carbide, their low mobility enhances charge trapping probability. Charge trapping and de-trapping broaden the distribution of (and protract) the times required for holes to reach the negative electrode.

Charge carrier motion within the depletion region causes the dominant detector output signal. The largest fraction of the depletion region extends into the silicon. The high purity of the silicon also enhances the probability of charge carriers avoiding capture by traps and recombination centers. These two factors improve the charge collection capabilities of the positive electrode, and justify collecting all spectra from

the n-side.

It is necessary for the charge collection time (16) to be smaller than signal processing time constant (Section 3.3.2) for the signal pulse to be a faithful measure of the energy deposited [14]. The charge collection times, $t_{collection}$, were approximated by (14 – 16).

$$\mathcal{E}(x) = \frac{qN_d}{\epsilon}(W - x) \tag{14}$$

$$v_n(x) = \mu_n \mathcal{E}(x) \tag{15}$$

$$\begin{aligned} t_{collection} &= \int_{x_0}^{0} \frac{1}{v_n(x)} dx \\ &= \frac{\epsilon}{q\mu_n N_d} \log \frac{W}{W - x_0} \end{aligned} \tag{16}$$

The electric field $\mathcal{E}$ during partially-depleted detector operation is not constant. The maximum electric field occurs at the p–n junction and then decreases linearly on both sides of the junction through the depletion region. The field vanishes at the depletion width boundaries. (16) assumes mobility is constant, and states that the collection time for charge created at $x_0$ is dependent on the drift velocity, $v_n$, which also varies with $x$ (distance from the depletion boundary). The values for electron mobility in Si, $\mu_n$, and hole mobility in boron carbide, $\mu_p$ are reported earlier in this section and in Table 1 respectively.

The charge collection time can also have significant effects on the transient current measured in the detector. The charge collection time represents the increment of time over which the deposited charge is integrated. The transient current, calculated from (17), must exceed the steady state leakage current in order to have a measurable pulse and good S/N ratios. The energy deposited, $E_{dep}$, is determined from the reaction Q-value, and $E_{pr}$, is the energy required to produce electron-hole pairs (3.6 eV in

silicon). $t_{trans}$ is calculated from (16), and $t_{plasma}$ is time needed to disperse the cloud of charged pairs such that they do not self-shield (2 – 5 ns) [14, 36]. Calculations shown in Appendix B.2 indicate that hole collection time is six orders of magnitude greater than the electron collection time.

$$I_{transient} = 2\frac{E_{dep}q}{E_{pr}(t_{collection} + t_{plasma})} \tag{17}$$

### 3.3.2 Signal processing component configuration

Before spectra were collected, the electronic connections and configurations of the detection electronics shown in Figure 24 were confirmed with a pulse generator. The pulser was connected to the oscilloscope and adjusted to deliver a 700 mV pulse. Each component was tested using the pulse generator signal. The final step in validating the equipment setup was to observe the pulser spectrum. The peak width (Figure 25) was only two channels, and centered just below channel 70. Channel 70 corresponded to an input voltage into the multi-channel buffer (with the conversion gain set to 1024 channels) of 700 mV. This agreed with the 700 mV oscilloscope pulse, and the fine width of the peak indicated that connections were correct, and that no observable electronic component-induced noise entered the detection circuitry. The specific settings and other pertinent information in reference to the electronic modules were listed in Appendix A.

Several preamplifiers were considered for this experiment and it is worthwhile discussing the factors leading to the final selection. The Ortec 142IH preamplifier is a charge sensitive universal purpose instrument that can be used for many classes of detectors including semiconductor detectors [42]. The instrument also accepts input from a bias supply to apply voltage to the detector. By this configuration, the diode bias is sent to the detector and the resulting response signal is delivered to the

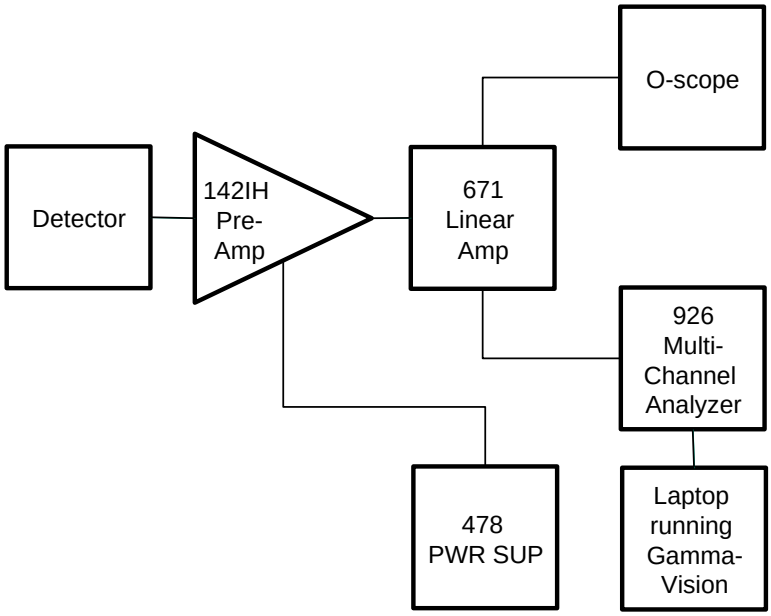


**Figure 24. Experimental procedure equipment connection diagram**

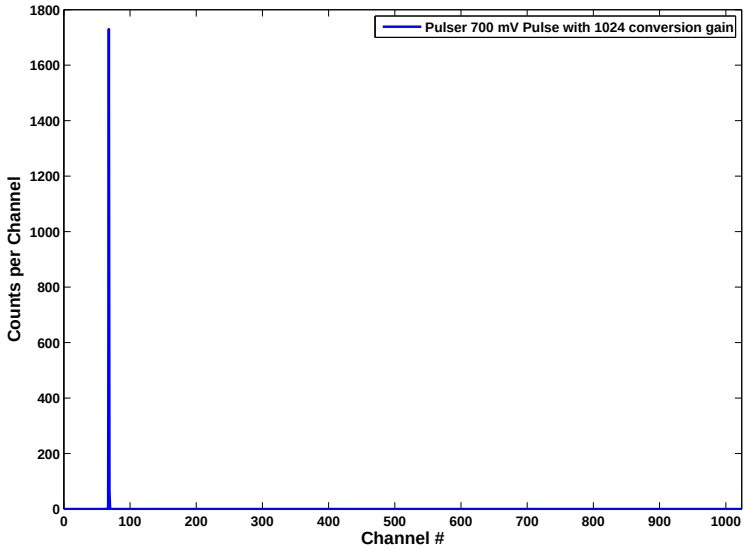


**Figure 25. Output spectrum for the pulser producing 700 mV pulse on oscilloscope.**

preamplifier input over the same cable.

The preamplifier time constant, $\tau$, was the determining factor in this experiment. The time constant is the product of the input impedance and dynamic capacitance, which for the 142IH are 93 $\Omega$ and 10,000 pF respectively [42]. The case where

($\tau >> t_c$) ensures that pulse generated is proportional to the charge deposited in the detector [14]. Appendix B.2 contains the values of $t_c$ and $\tau$ with the appropriate calculations. Calculations in Appendix B.2 indicate collection times on the BC side were greater than the time constant.

The background spectra were collected for each detector prior to placing it near the source. Spectra were then measured for 300/600/900 s while being irradiated by the neutron source. A low level discriminator was used to ensure dead time did not exceed 10%. Once complete, a cadmium foil was wrapped around the aluminum case and an additional 300 s spectra was collected. The pulse-height spectra from UMKC diode showed spectral features with these spectra duration times but due to the low energy of the pulses, the interference from background was significant. An additional set of spectra was collected for UMKC diode only, but the duration times of the spectra were increased to 600/1800/3600 s.

### 3.3.3 Neutron source

The neutron irradiation experiment was performed at The Ohio State University Nuclear Reactor Lab. A 5.0 Ci Plutonium-Beryllium (PuBe) source was used as a source of neutrons. The PuBe source contained a mixture of Pu and Be. The source was sealed in an 15 gallon steel drum filled with borated-parrafin. A central cavity of the "neutron howitzer" was hollow and lined with a 7 $^5/_8$" diameter aluminum pipe. The PuBe source was stored inside that aluminum pipe, and no moderating material was placed above the source in the original configuration [43]. Two 1-in discs of polyethylene were placed between the source and the detector while spectra were collected.

Plutonium decays and produces *alpha* particles and uranium (18 – 19). Beryllium absorbs those $\alpha$'s and produces carbon and neutrons (22). Additional neutrons born

from (21) increase the neutron emission rate for several years after the production of the source [44].

$$^{239}_{94}\mathrm{Pu} \longrightarrow {}^{235}_{92}\mathrm{U} + {}^{4}_{2}\alpha \tag{18}$$

$$^{238}_{94}\mathrm{Pu} \longrightarrow {}^{234}_{92}\mathrm{U} + {}^{4}_{2}\alpha \tag{19}$$

$$^{241}_{94}\mathrm{Pu} \longrightarrow {}^{241}_{95}\mathrm{Am} + \beta^{-} \tag{20}$$

$$^{241}_{95}\mathrm{Am} \longrightarrow {}^{237}_{93}\mathrm{Np} + {}^{4}_{2}\alpha \tag{21}$$

$${}^{9}_{4}\mathrm{Be} + {}^{4}_{2}\alpha \longrightarrow {}^{1}_{0}\mathrm{n} + {}^{12}_{6}\mathrm{C} \tag{22}$$

Use of the Bateman equations is required to calculate the neutron emission rate for (18) thru (22). The neutron emission rate calculation, modified from [45], is included in Appendix B.3. Figure 26(a) shows that the PuBe neutron spectrum is predominately fast neutrons, with the largest peak centered at 4 MeV [46]. The curve maximas in Figure 26(b) correlate to the thickness of polyethylene required to thermalize a beam of mono-energetic neutrons [47]. The dashed green corresponds to 1 MeV fast neutrons, which become thermalized after penetrating 3.0 cm of polyethylene. By interpolating, 4.0 cm of polyethylene (1.08 cm less than the thickness of the two polyethylene discs used during the experiment) is an ample thickness for moderating most of the PuBe source neutron population.

The geometry of the experiment is shown in Figure 27. Neutrons emitted were captured by the borated-paraffin unless they were emitted vertically upward through the void in the parraffin directly above the source. The detector was therefore placed 8 inches above the source. Activity was calculated at $1.19\times10^{7}$ [n $s^{-1}$]. With the known isotropic neutron emission rate, the thermal flux at the detector location as well as the rate reaction density could be calculated (included in Appendix B.3).

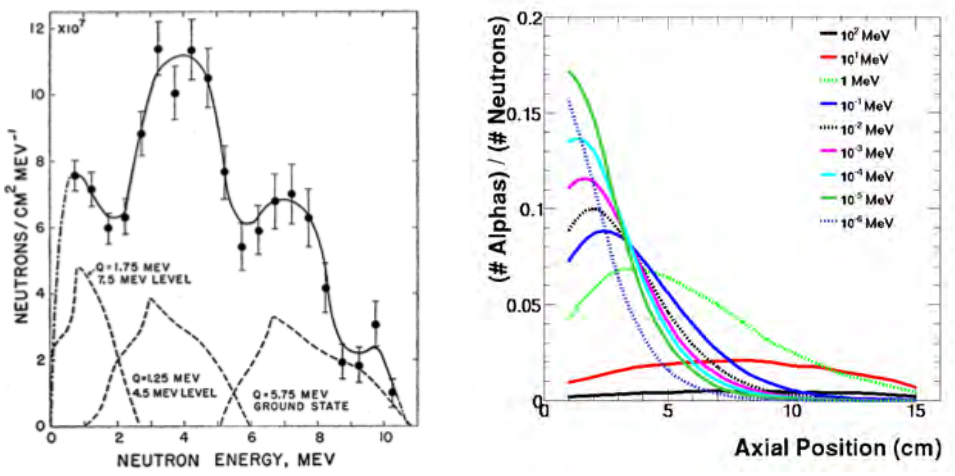


(a) (b)

**Figure 26. (a)PuBe neutron spectrum [46]. (b) Thermalization as a function of polyethylene thickness [47].**

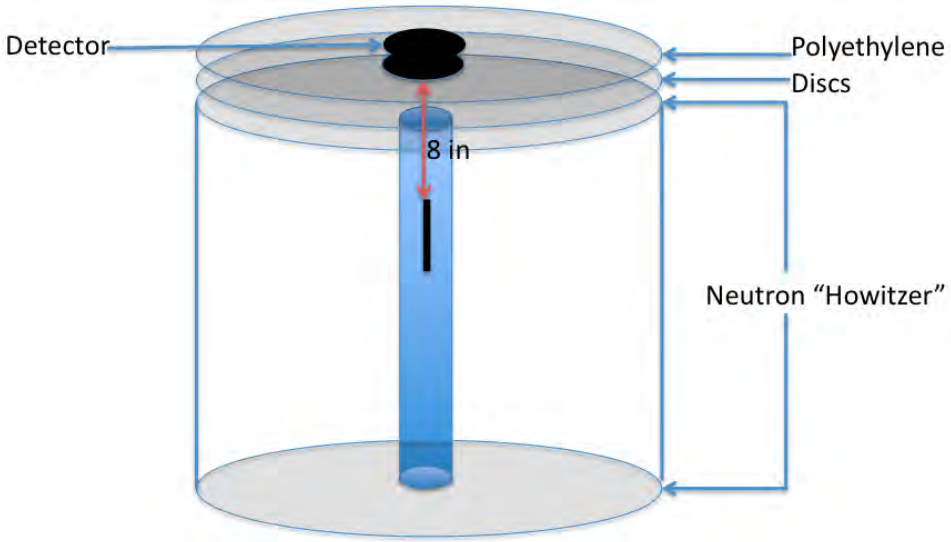


**Figure 27. Geometry of the irradiation experiment using a PuBe source. The source and detector were separated by eight inches (including two inches of polyethylene).**

$$\Phi_{th} = \frac{\mathcal{A}\mathcal{B}\Omega}{4\pi} \tag{23}$$

$$\Sigma = \sigma_{th} N \tag{24}$$

$$RRD = \Sigma \Phi_{th} \tag{25}$$

The thermal flux was estimated using (23), where $\mathcal{A}$ is the neutron emission rate and $\mathcal{B}$ is the branching ratio for the reaction of interest. From (1), the branching ratio was 94%. $\Omega/4\pi$ is the probability that the source neutron hits the detector, and $\Omega$ is the the solid angle subtended by the detector [48]. The thermal macroscopic cross section, $\Sigma$, is given by (24), where $\sigma_{th}$ is the microscopic thermal capture cross section and $N$ is the atomic density. Given a thermal flux of 464 [n/cm$^2$–s], the reaction rate density was then computed as $1.14\times10^7$ [cm$^{-3}$ s$^{-1}$].

# IV. Results and Analysis

## 4.1 Irradiation Results

None of the devices used in this study produced spectral features or oscilloscope traces that could be linked to neutron capture events. The UNL resistive device spectra had some features, but the increased pulse amplitudes and frequencies observed in the oscilloscope while the device was shielded by a cadmium foil conclusively indicated that neutron capture products were not producing the observed signal.

The UMKC diode did not produce spectra with identifiable features. Pulses observed on the oscilloscope indicated the possibility of an interaction, but when compared to the pulse height spectra, it was apparent the pulses were due mostly to noise and gamma/X-ray interference. Recall that the UMKC diode exhibited diode-like C–V characteristics but pre-characterization measurements also indicated high leakage currents ($\approx$10 $\mu$A at 5.0 V reverse bias) and large capacitances. These two undesirable properties of the diode likely contributed to the failure to detect thermal neutrons.

The UNL diode did not yield a single useable spectrum. The 300 s measurement totaled more counts in several of the low energy bins than the 900 s measurement. The pulse amplitudes did not exceed 400 mV, and thus each pulse was tallied at or below channel 40. A constant fluctuation in the noise baseline was observed on the oscilloscope, most likely due to changes in the leakage current.

### 4.1.1 UNL resistive device

The most interesting resistive device spectral feature was the broad peak centered at approximately channel 500. In Figure 28(a), the x-axis corresponds to the channel, or energy bin number. The multichannel analyzer measures each incoming pulse

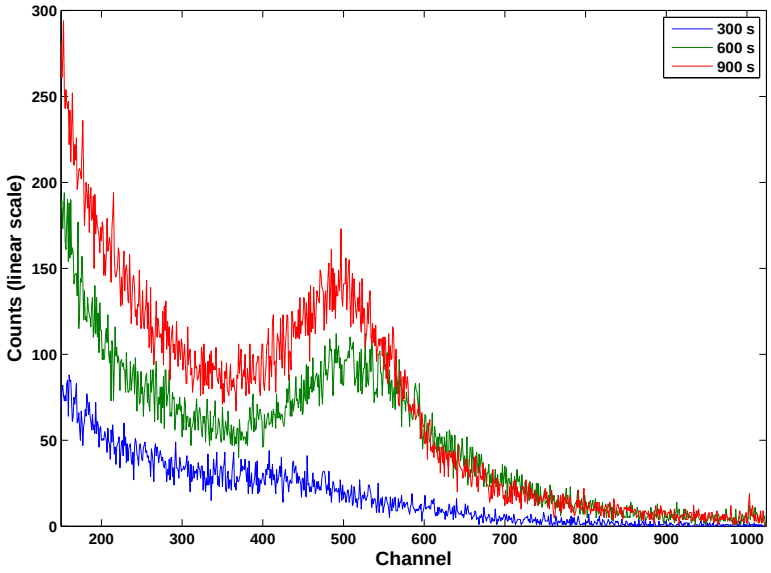


(a)

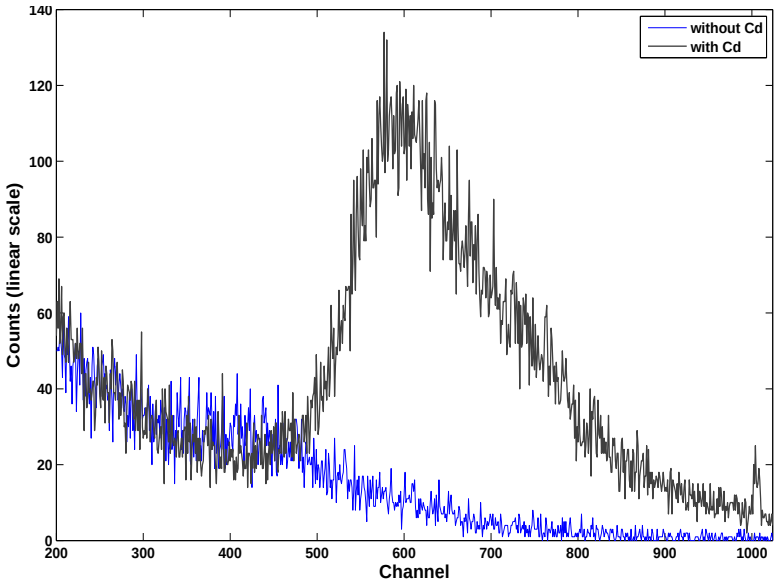


(b)

**Figure 28. (a) UNL resistive device pulse height spectra with 300/600/900 s durations. (b) The number of total counts increased and the dominant peak shifted to the right 100 channels, meaning the amplitude of the pulses from the detector had increased with cadmium shielding.**

height, assigning the height to one of many pulse height ranges. The spectra shown in Figures 28(a) and 28(b) used a conversion gain setting of 1024. This meant the 10.0 V effective range of the multichannel analyzer was divided into 1024 equal groups,

or bins. Once the incoming pulse was properly assigned to an energy bin, a counter incremented the corresponding channel's count number.

The peak observed was first believed to be one, or two, full energy peaks from the $^{10}$B(n, $\alpha$)$^{7}$Li reactions. Although the peak was somewhat less obvious for the 300 s duration measurement, it was plainly visible for the 600 and 900 s spectra. The centroid of the peak shifted slightly for the longer measurement, but its shape was well-preserved, and the total number of counts under the peak increased for the longer measurements. The large width of the peak was consistent with lower charge carrier mobilities expected from resistive detectors that would broaden the charge collection time distribution.

The device was wrapped in a cadmium foil, and a pulse height spectrum was collected for 300 s. The counts under the spectral peak, and the total counts for the entire spectrum increased. The centroid of the peak also shifted to a higher energy group. These three observations indicated that the peaks observed were induced by something other than a neutron-induced reaction.

It is possible that thermal neutron interactions occurred in spite of the cadmium shielding. Fast neutrons can deposit energy in the foil and reach thermal equilibrium through elastic scattering before interacting with the detector. This occurrence, although possible, is improbable and is not a realistic explanation for the increase in the observed count rate. This increase in the count rates and peak intensities leads to one valid conclusion. Neutron capture reaction products are not responsible for the observed pulse-height spectrum peak.

Cadmium absorbs thermal neutrons by (4) and emits high energy $\gamma$'s. This can cause Compton scattering with gadolinium ($\sigma_{compton}$=22.7 b [7]), which produces low energy gamma/X-rays that can produce pulses within the resistive bulk. Another, and potentially more likely explanation can be linked the the PuBe neutron spec-

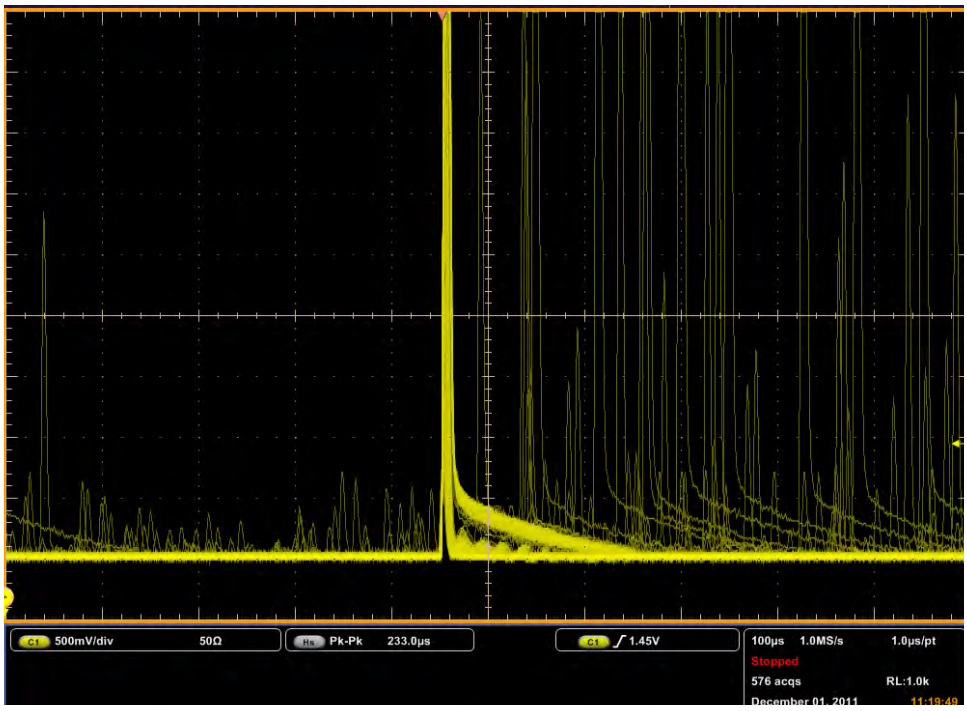


**Figure 29. Scope trace (infinite persistence) of the UNL Resistive Device being irradiated by PuBe source.**

trum. Elastic and inelastic scattering occurs within the cadmium, and as reported by [44], the population of photons below 20 keV increases due to down-scattering in the cadmium. Because lower energy photons have an increased probability of interaction within the detector, this is a logical explanation for the data collected from this resistive device. Additionally, the gadolinium Compton scatter cross section for 20 keV photons ($\sigma_{compton}$=20.7 b [7]) would also facilitate an influx of low-energy photons capable of depositing energy within the detector.

The pulse traces were observed from an oscilloscope (Figure 29) during the irradiation and a persistent 4.0 – 5.0 V pulse occurred several times a second. The device was only biased to 90.0 V, but the goal was to apply greater voltages (up to 700 V) in order to rapidly sweep any neutron induced charges towards the collecting electrode. The high voltage supply was set to the maximum output yield but the resistance across the preamplifier circuit greatly attenuated the bias strength. The apparent

noise observed on the oscilloscope increased with bias as well. Upon considering the pulse height spectra collected, improving the electrical configuration was declined due to the disadvantageous effect of gamma/x-ray interference.

The pulse shown is characterized by two features. The first and and most prominent feature is the large amplitude pulse, with a short rise time. This is characteristic of the fast timing properties of fully-depleted semiconductor detectors. The device was resistive and depletion was not expected. These large peaks with short rise times are likely due to the fluctuating leakage current of the device. The pulse tail shape does however resemble the expected pulse shape. The high resistivity of device would naturally reduce the charge carrier drift velocity and increase charge collection times, which is consistent with the small-amplitude but broad peak observed on the oscilloscope.

### 4.1.2 UMKC diode

The UMKC diode, like the UNL resistive device, experienced some interaction when placed over the PuBe source. Oscilloscope pulse traces showed a 700 mV peak was present with an approximate frequency of once every 5 s. Pulse height spectra on the other hand did not show any distinct features, and thus a second collection iteration was performed. Pulse-height spectra for 600/1800/3600 s were collected in order to increase the overall number of counts, and the conversion gain setting on the multichannel buffer was reduced to 512 channels. The linear amplifier gain was also adjusted to produce a 5.0 V output pulse from the preamplifier (observed on the oscilloscope).

Increasing the time duration for the spectra, and increasing the amplifier gain did not result in improved spectra with identifiable features (Figure 30(a)). Cadmium shields again were used to help discriminate between interactions that were neutron

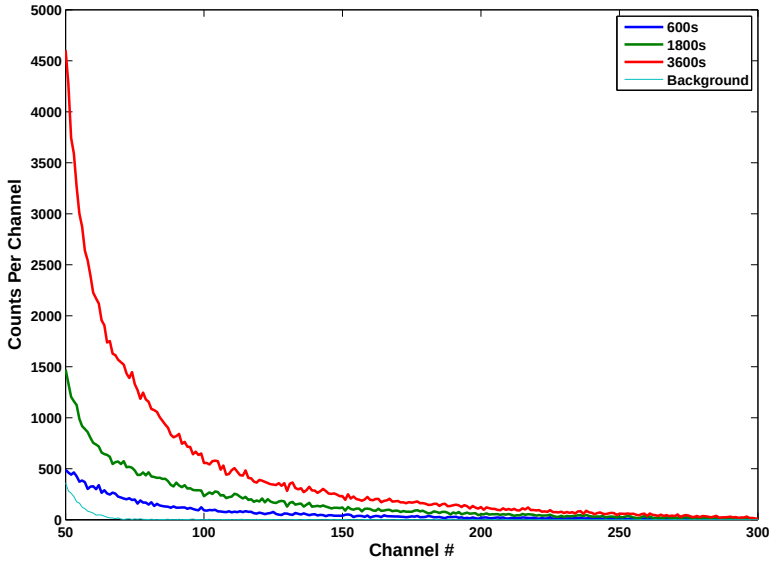


(a)

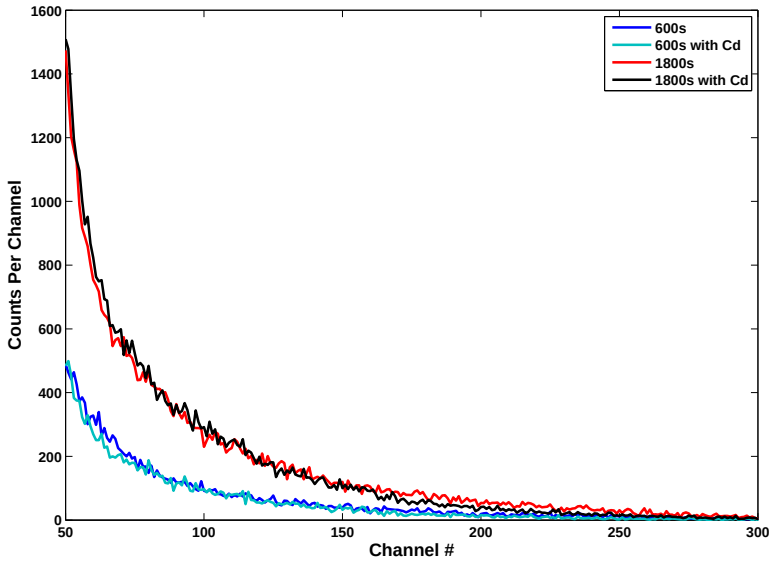


(b)

**Figure 30. (a) UMKC diode pulse height spectra with 600/1800/3600 s durations. (b) No change observed with cadmium foil.**

induced and those that were not. The cadmium foil had no effect on the spectrum (Figure 30(b)). The spectra collected with and without the cadmium shielding overlapped, meaning the total number of counts per channel remained relatively constant. The absence of any spectral feature however could not alone invalidate the hypothe-

sis central to this research. Hetero-junction diodes containing neutron-sensitive constituents may be able to detect neutrons, but the electronic and material properties may only produce signals above the noise threshold with precisely optimized geometries and fabrication procedures.

The pulses observed in the oscilloscope (Figure 31) were the result of some effect occurring in the detector induced by the PuBe source. Background oscilloscope traces did not show these pulses or any type of signal other than small fluctuations in the noise baseline. Persistence was enabled (10 s variable persistence) as a means of comparing the pulse amplitudes. The overlapping peaks shown in Figure 31 have amplitudes ranging from 2.0 – 5.0 V. This continuum of peak heights caused higher channel counts on the pulse height spectra, but the distribution did not favor any one particular energy. Thus, no features were apparent on the pulse height spectra in spite of the oscilloscope output.

The leakage current increases noise baseline. The leakage current can also fluctuate, and this is known source of noise in semiconductor detectors [14]. This effect exists in both bare and cadmium shielded spectra, and it could be responsible for the observed activity on the oscilloscope.

The pulse shape of partially-depleted detectors is characterized by two features. The induced depletion current contributes to the fast rise time and large pulse amplitude [49]. Detectors operated at or above saturation have constant electric fields throughout the device and carrier transport is a drift process only, and hence the charge collection times are small. In partially depleted detectors, the charge carrier transport occurs by both drift and diffusion processes. The vanishing electric fields cause a reduced drift velocity as carriers migrate toward the electrode, resulting in drawn-out pulse tails [16].

Recall from Figure 20(a), the UMKC diode was depleted less than 10% into the

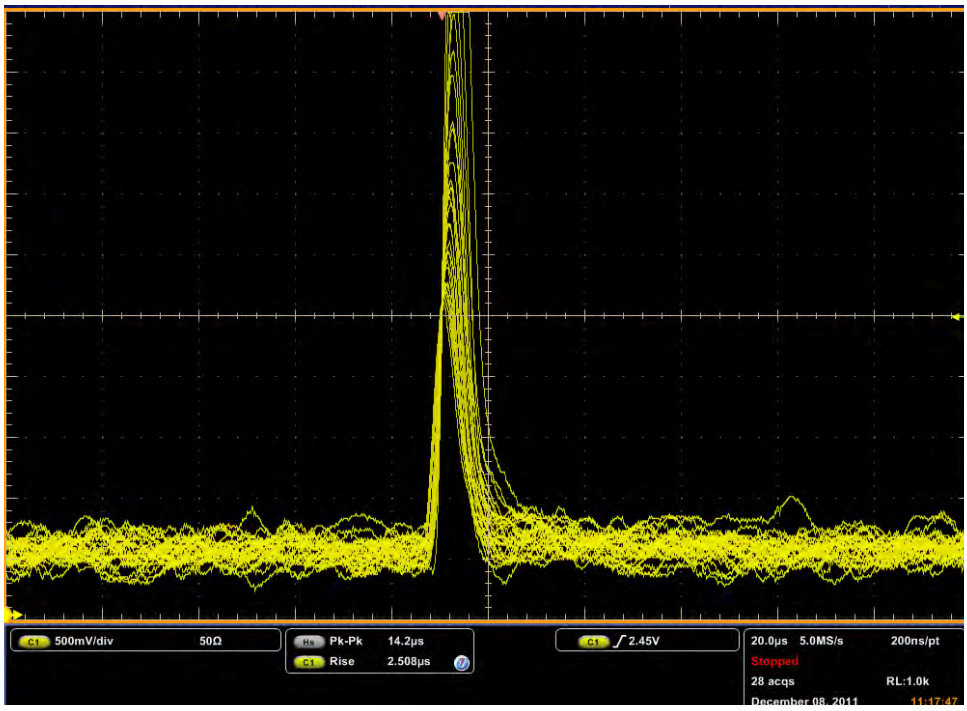


**Figure 31. Scope trace (infinite persistence) of the UMKC diode being irradiated by PuBe source.**

silicon. Pulse tails would be expected with this limited amount of depletion, and their absence in the oscilloscope output was a clue that the observed pulses on the scope were not related to ionized charge transport through the detector.

Neutron capture products were created in the boron carbide region, and caused ionizations in the depleted silicon. It is also feasible that the induced signal was below the minimum detectable limit of the collection electronics. The drift-induced contributions to the current pulse were adversely affected by low electric fields. Once charge entered the un-depleted bulk region of the silicon, the electric field was no longer present and carrier transport occurred via diffusion only.

The maximum charge collection length in partially depleted detectors is given by

$$L_F = \left[ 2L_{diff} + \left( 1 + \frac{\mu_n}{\mu_p} \right) W \right], \tag{26}$$

where $L_{diff}$ is a length by charge diffusion [50]. Large diffusion lengths contribute to longer carrier lifetimes and enhance charge collection probabilities. The diffusion length is given by (29) and (27) is used to calculate the minority carrier mean free time. The diffusion length in n-type silicon is determined by the minority charge carrier type, which is denoted by the $p$ subscript in (27 – 29).

$$\tau_p = \frac{m_p \mu_p}{q} \tag{27}$$

$$D_p = \left(\frac{kT}{q}\right) \mu_p \tag{28}$$

$$L_{diff} = \sqrt{D_p \tau_p} \tag{29}$$

The carrier lifetime, $\tau_p$, is determined from the hole mobility and effective mass, $m_p$. In silicon, the effective mass $0.69m_0$ where $m_0$=$0.91\times10^{-30}$ kg. The diffusion coefficient, $D_p$, is determined from (28), which is known formally as the Einstein relation [15].

The diffusion length calculation (Appendix B.1.1) gives a diffusion length of 1.4 $\mu$m. With the silicon only depleted 44.5 $\mu$m from the junction, (26) yields a charge collection length slightly less than 25% of the silicon wafer thickness ($L_F \approx 180$ $\mu$m). This also implies the induced charge decays significantly once swept through the depletion region and probability of absorption prior to being collected by the electrode is great.

Both the insufficient depletion width and total charge collection length (26) were likely causes for the absence of any detector response. A simple device model was created to analyze the detector charge collection capabilities and efficiencies. Geometric parameters of the diode, such as the silicon and boron carbide thicknesses, and the biases applied to the electrodes were varied in order to identify factors which contributed to the negative detector response.

## 4.2 Diode Modeling

Davinci is a device simulation program that models the behavior of wide variety of semiconductor devices, including hetero-junction diodes, in two or three dimensions. The software numerically solves Poisson's equation and both continuity equations (electrons and holes) in order to analyze the device's electrical characteristics at an arbitrary bias. Due to the complexities of semiconductor devices, the solutions to this system of three partial differential equations are rarely obtained analytically. Analytical solutions are also only achieved after several simplifying assumptions have been made. Davinci discretizes the three equations over a nodal grid and produces accurate solutions to them.

The specific objective of the modeling was to replicate the irradiation experiment described above. The depletion width and saturation current were affected by varying user-defined parameters in order identify the source of the device's failure in producing a signal. Davinci replicated the ionization caused by energetic charged particles within that depletion region, and produced a time-dependent transient solution. Using transient solution outputs, the induced charge, potential, and current were calculated at the collecting electrodes. The initial step in the modeling was the creation of a diode and mesh that replicated the I–V characteristics of the actual physical diode. This was then followed by heavy charged particle ionization simulation. The depletion widths were then extended further into the silicon by increasing the reverse bias. The diode geometric parameters were also varied in order to conduct a small-scale optimization study and determine which factor played the greatest role in causing the negative detector response.

### 4.2.1 Creating the diode and mesh

Figure 32 illustrates the 3D representation of the modeled diode. Only a small section of the diode could be replicated in Davinci due to the limited number of available nodes. The width of the diode was retained in order to give fidelity to model-generated output. The suspected issue with the diodes was the excessive silicon width, and the inability to adequately deplete it or deliver charge to the electrodes.

Amorphous boron carbide was not available as material within the Davinci library. The generic semiconductor (SEMICOND) was used as the base material and its default properties were modified according to Table 6 so that the diode was a realistic representation of the physical diode used during the actual experiment. $N_A$ values in Table 6 were based on [31] conflict with Table 4, whose values correspond to calculations performed after the device modeling was completed. Despite this discrepancy, the modeled device had a larger depletion region than was determined from experimental data. With the modeled diode's enhanced depletion and hence, greater detector volume, the simulation of heavy charged particle ionization nevertheless failed to represent sufficient charge to be detected above intrinsic noise of the Ortec 142IH preamplifier. For this reason, the conclusions drawn from the model are still considered relevant and valid.

### 4.2.2 Model versus physical device comparison

The simulated diode current density characteristics are shown in Figure 33(a). J–V was a means for comparing the characteristics of two geometrically dissimilar diodes. The reverse bias current density in the model approached the magnitude of the physical diode reverse current density by a factor of 2.3, and within a factor of 1.3 of the theoretically computed saturation current density from (8). The diode also replicated the sub-linear forward current behavior discussed in Section 3.2.1. At low

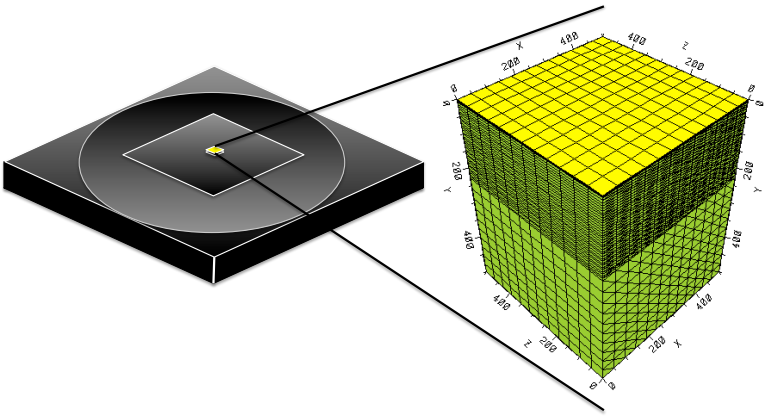

**Figure 32. 3D plot of the diode created in Davinci. The 500 × 500 × 500 $\mu$m$^3$ Davinci model essentially represents just a small section of the physical diode (illustrated by a small cube extracted from the center of the aluminum contact). The disc-like surface represents the boron carbide deposition on the n-type silicon.**

**Table 6. Material parameters for Davinci model**

| Parameter | Silicon | Boron Carbide |
|---|---|---|
| Semiconductor Material | Silicon | SEMICOND |
| Profile | N-Type ($10^{11}$) | P-Type ($4.2\times10^{12}$) |
| Bandgap | Default | 0.9 [eV] |
| $\tau_{n0}$ | $10^{-7}$ [s] | $10^{-8}$ [s] |
| $\tau_{p0}$ | $10^{-6}$ [s] | $10^{-8}$ [s] |
| Permittivity Constant | Default | 8 |
| Affinity | Default | 4.58 [36] |
| $N_C$ | Default | $10^{19}$ [cm$^{-3}$] |
| $N_V$ | Default | $10^{19}$ [cm$^{-3}$] |

biases, the modeled diode exhibited immeasurably small currents. However, the J–V characteristics at 5 V reverse bias, the same conditions set during the irradiation phase of this experiment, adequately replicated the actual diode. Therefore, it was inferred that individual parameters of this model could be adjusted, and corresponding effects on the virtual device would be the same, at least qualitatively, to similar modifications of the actual diode parameter.

The diode electric field decreases linearly from the junction (Figure 4). The field

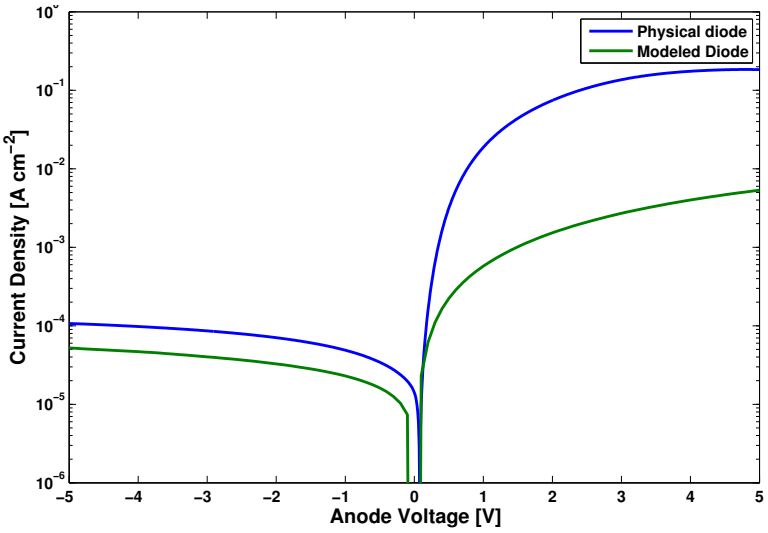


(a)

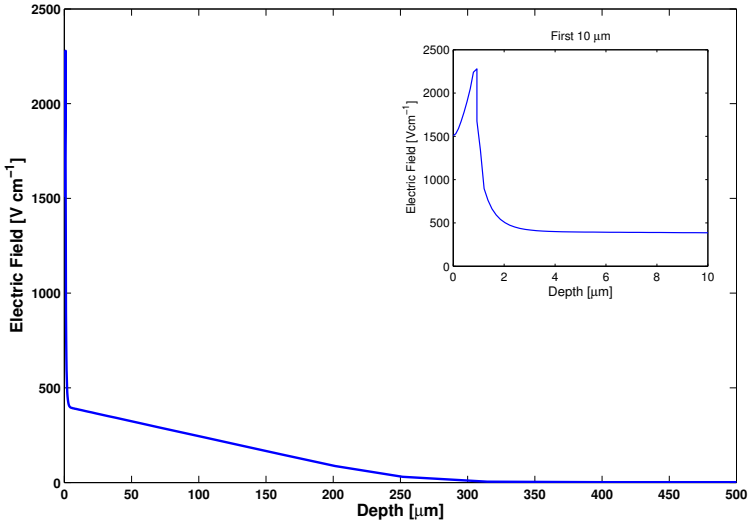


(b)

**Figure 33. Davinci simulation of (a) current density (J–V) and (b) electric field at 5 V reverse bias. The inset is a close-up view of the the first 10 microns of the diode (starting from the boron carbide surface).**

extends to a depth that contradicts calculations presented in Appendix B.1.1 predicting approximately 45 $\mu$m of depletion at 5 V reverse bias. The electric field is initially zero on the p-side contact and rapidly increases to the maximum field strength value of 2156 [V/cm] at the junction. From the peak electric field at the junction and extending towards the silicon, the electric field becomes discontinuous and drastically

decreases in strength by a magnitude of 1400 [V/cm] within the first 4 microns into the silicon. The inset in Figure 33(b) shows this discontinuity caused by the differences in the semiconductor permittivities. Following the sharp decrease, the electric field drops linearly, as expected, until it decays almost completely at 300 $\mu$m into the silicon.

### 4.2.3 Heavy particle ionization simulation

The purpose of this phase of the modeling was to observe the transient output on the positive (n-side) electrode once a virtual heavy charged particle was injected into the silicon. Some simplifications were necessary to allow for the simulation to proceed, and without excessive run times. First, the particle track was assumed to follow a straight line parallel to the y-axis of the diode and originate at the the coordinates (x, y, z) = (0, 0, 0). The column of charged particles was assumed to have a Gaussian radial dependence. The temporal generation dependencies were also assumed to be Gaussian.

The $\alpha$ particle had the greatest kinetic energy. Therefore, it caused the most ionizations and with the longest ionization track length through detector. The energy deposited in the detector was thus based on the $\alpha$ stopping power of silicon. Charged particle injection was simulated through the PHOTOGEN command.

User-defined parameters provide the ability to customize the simulation and control the amount of charge injected and from where. PHOTOGEN also provides the option to call a linear energy transfer file in order to prescribe the amount of charge deposited as a function of depth. This energy transfer table originates from $\alpha$ stopping power data [51], and (30) facilitates a conversion to pC/$\mu$m. The values are then

in a form that is compatible with Davinci.

$$LET = \frac{dE}{dx} \text{ [MeV cm}^2 \text{ g}^{-1}\text{]}$$
$$L_f(l) = \int_0^l \frac{LET\ \rho}{\epsilon_i\ /q} dx \text{ [pC } \mu\text{m}^{-1}\text{]} \tag{30}$$

In (30), $\rho$ is the density of silicon (2.33 [g cm$^{-3}$]), and $\epsilon_i$ is the ionization energy of silicon. A MATLAB script interpolates the table values, and iteratively decrements the particle energy for every 0.1 $\mu$m ($dE = dE/dx\ \Delta x$) so that the linear energy transfer values can be obtained with respect the depth into the silicon. The output of the script is plotted in Figure 34.

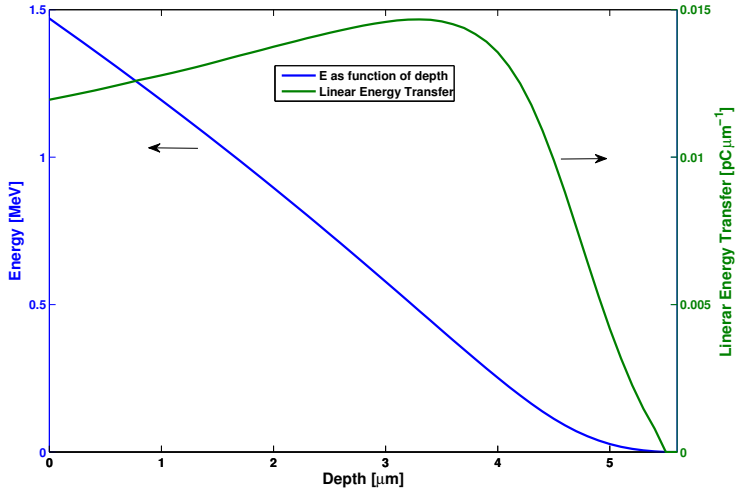


**Figure 34. Particle energy and LET in silicon as a function of depth. The left ordinate corresponds to the particle energy (shown in blue); the right ordinate corresponds to the LET in silicon.**

The charge generation function has linear dependency, as well as time and radial dependence. Davinci simulates a Gaussian radial and temporal charge distribution by (31), and (32) respectively.

$$R(r) = \exp\left[-\left(\frac{r}{DCHR}\right)^2\right] \tag{31}$$

In (31), $r$ is the radius and $DCHR$ specifies the characteristic radial charge distance[52]. Simulation using the TRIM code report that 5 nm is the characteristic radial charge distance of 1.47 MeV $\alpha$ particles in silicon [36]. A mesh scheme with such a fine spacing was impossible due to the size of the device and node limitations invoked by the software. The characteristic radial distance was increased to 0.2 $\mu$m in order to prevent excessively long run times. In (32), $T0$ and $TC$ are the offset time and pulse generation time respectively. The offset time is arbitrarily chosen, and the pulse generation time is $1.9\times10^{-12}$ s (calculated from stopping power data).

$$T(t) = \frac{2\exp\left[-\left(\frac{1-T0}{TC}\right)^2\right]}{TC\sqrt{\pi}\ \mathrm{erfc}\left(-\frac{T0}{TC}\right)} \tag{32}$$

Figure 35 is the time-dependent transient solution for a single $\alpha$ particle depositing its energy within the active region of the detector. The current shown was adjusted to account for differences between the virtual and the physical diode cross-sectional areas. The magnitude of the pulse was compared to the estimated leakage current, and the pulse was also integrated to calculate the total charge induced on the electrodes. Both of these calculations were simplified by correcting the current to account for the cross sectional area differences instead of using the current density. The pulse peaked in less than 10 ps, before decaying. The current then continued increasing until it reached the steady-state reverse bias current.

Drift velocity is proportional to the electric field (15), and given the low field strength (Figure 33(b)) in this diode, the collection time is orders of magnitude larger than initially calculated. The transient current is given by $dQ/dt$, and as collection times become long, the transient currents become smaller. Another point of consideration is the enhanced recombination and trapping that occurs with decreased drift velocity.

One conclusive measure of whether or not the pulse was detectable was to com-

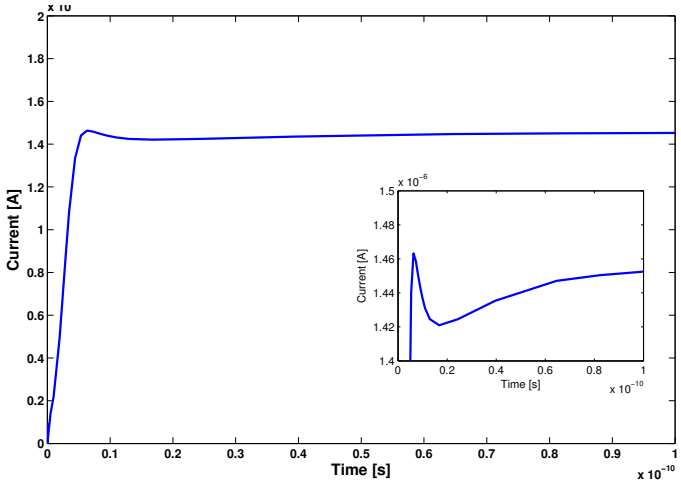


**Figure 35. Simulated pulse output for a simulated diode using the Davinci transient solution mode. The time-dependent solution is computed following a simulated injection of charge via the PHOTOGEN command.**

pare the total induced charge with the intrinsic noise charge of the charge-sensitive preamplifier used during this experiment. The preamplifier intrinsic noise level,

$$\text{FWHM (noise)} = 2.35\epsilon\frac{V_{RMS}}{V_p}, \tag{33}$$

is commonly reported as a function of input capacitance. For the case of this experiment, the intrinsic noise level was 4.6 keV[42]. $\epsilon$ is the amount of energy required to create one charge carrier (3.6 eV for silicon), the $V_{RMS}/V_P$ is the intrinsic noise charge[53]. The intrinsic noise charge calculated via (33) reached $2.04\times10^{-16}$ C. The total induced charge was calculated by (34) where $Q$ was the total induced charge, $t_c$ was the charge collection time, and current $I(t)$ was a function of time.

$$Q = \int_0^{t_c} I(t)dt \tag{34}$$

The total induced charge ($4.67\times10^{-17}$ C) did not exceed the intrinsic noise charge of the preamplilifier. This meant the charge detection capability of the preamplifier was

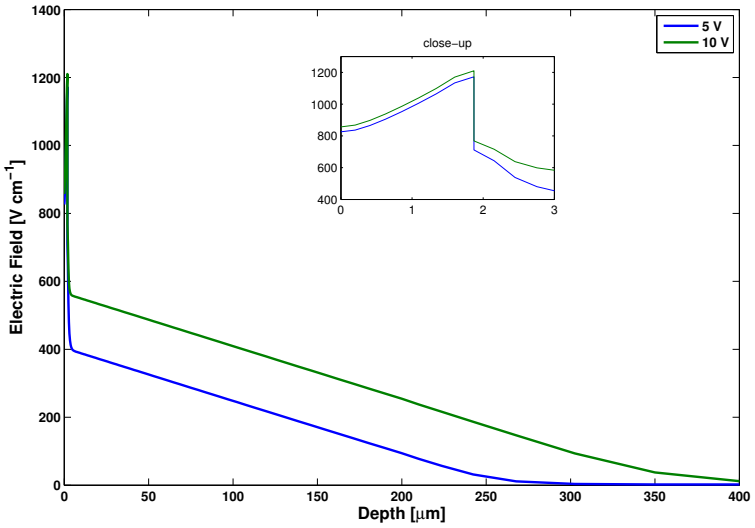


(a)

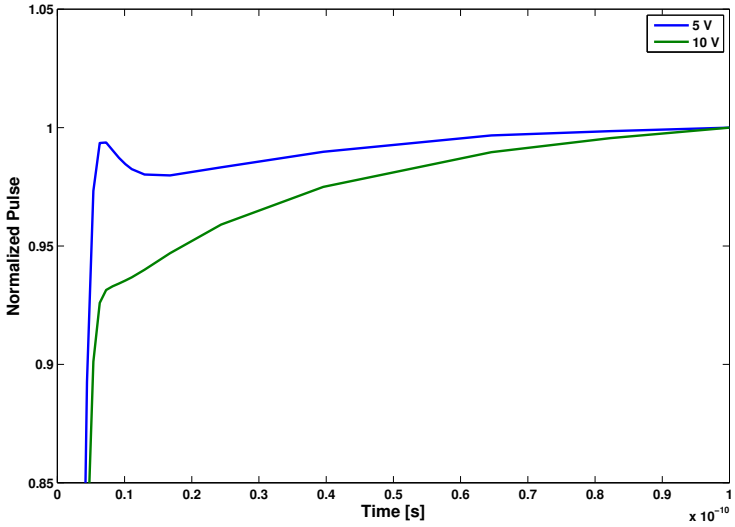


(b)

**Figure 36. Davinci simulation showing the effect of bias on (a) the electric field (the inset figure is an expansion of the top 3 microns) and (b) the transient current.**

not sensitive to the quantity of induced charge resulting from the neutron capture. Figures 36(a) and 36(b) investigate the device's electric fields and pulse outputs with 100 microns of silicon removed. Additionally, the width of the boron carbide was doubled. Increasing the amount of boron carbide theoretically would increase the degree of depletion in the silicon region, but the opposite effect resulted from the

geometry just described. The electric fields decreased as a result of increasing the boron carbide thickness. The pulses generated from the Davinci transient solution showed a suppressed peak at 5 V reverse bias. The pulse did not exceed the steady state saturation current with 10 V reverse bias applied. Boron carbide and silicon

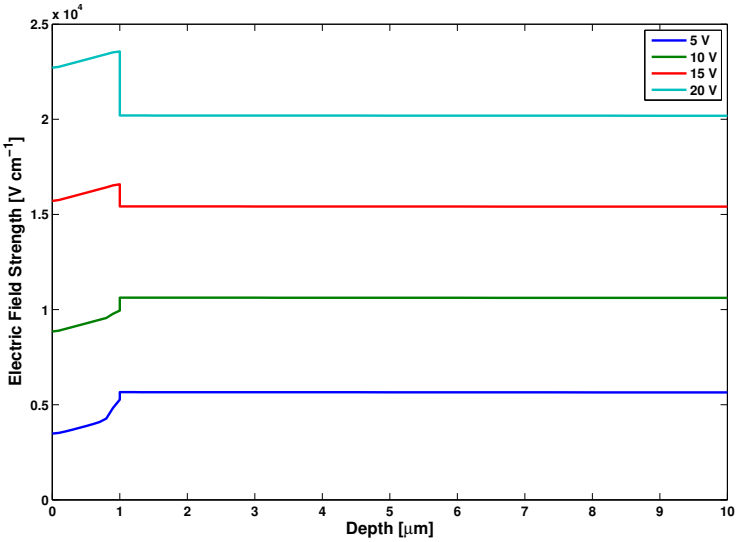


(a)

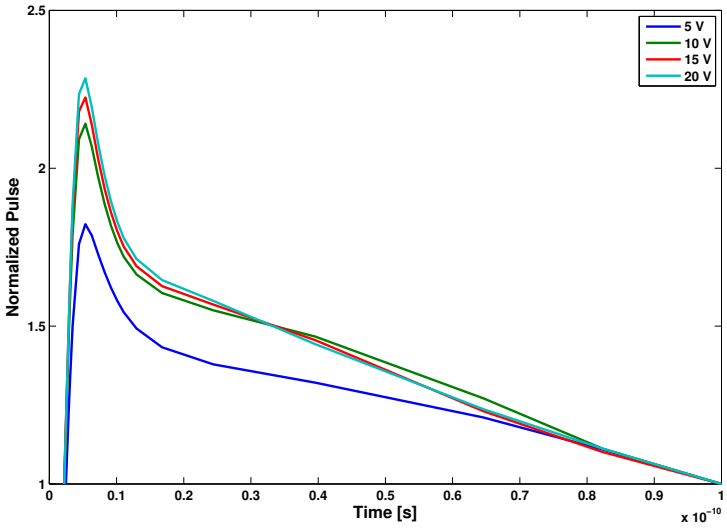


(b)

**Figure 37. (a) Electric field and (b) transient current with only 10 microns of silicon.**

effective doping concentrations, the particle strike origin, and particle direction were also examined to determine what effect, if any, they had on the detector performance.

After a completing multiple simulations, the electric field strength was the only factor that noticeably affected the diode charge collection ability and the resultant transient current. This conclusion was supported in Figures 37(a) and 37(b). The diode used in this simulation contained a 1 micron thick boron carbide region and a 10 micron silicon region.

This diode was depleted beyond the saturation point, and the electric field was large and constant throughout the silicon. The transient solutions were normalized in order to account for the different steady state currents at 5.0 – 20.0 V reverse bias. At 5.0 V reverse bias, the transient current pulse was 1.78 times greater than the reverse bias current; at 20.0 V reverse bias, the transient maxima reached 2.25 times the magnitude of the steady-state current. It was clear that electric fields in the UMKC diode were too weak and the resultant slow drift velocities hindered the charge collection efficiency by increasing the charge collection times and the probability of recombination and trapping.

# V. Conclusion

## 5.1 Experimental Findings

No experimental evidence of neutron detection was observed during the course of this experiment. The devices were introduced into thermal neutron environments with a calculated total neutron flux of 464 [n/cm$^2$–s]. Neutrons interacted within the diodes, but no corresponding signal was identified on either the oscilloscope or the pulse-height spectra. The root cause of a failed detector response was investigated through modeling.

The following summarizes the findings from this research:

1. The UNL resistive device exhibited behavior entirely opposite to the anticipated response to shielding the device with a cadmium foil. The pulse magnitudes and intensities increased with the addition of the cadmium shield. This was a clear indication that the observed peak in the pulse-height spectra was caused by interactions other than thermal neutron capture. The cadmium-covered device also demonstrated the device's gamma sensitivity.

Cadmium is a high Z element and can soften the PuBe photon spectrum by down-scattering and the result is a higher flux of photons below 20 keV. Since lower energy photons have a higher probability of interacting with the detector, it is likely that this was a source of photon interference observed in the oscilloscope while the detector was being irradiated. Additionally, cadmium absorbs thermal neutrons and re-emits 263.5 keV gamma rays as a product of the radiative capture reaction. Gadolinium, which is also a high Z material, has a Compton scatter cross section of 20.1 b and 22.7 b for 20.0 and 263.5 keV photons respectively. The gadolinium oxide film may have enhanced the device's photon sensitivity by down-scattering the photons and

increasing the population of photons depositing energy within the detector.

2. The UNL diode junction was likely damaged during the course of experiments performed previously. Useable pulse-height spectra could not be obtained from the diode. Pre-characterization of the device showed the device's C–V characteristics deviated from the expected junction behavior. This was the first indication that problems persisted within the diode, and it was not surprising that diode performed poorly while being irradiated. The dopant concentrations $N_A$ and $N_D$ could not be calculated from the measured C–V data, and thus a theoretical reverse saturation current density was not approximated. The diode was less conductive than the UMKC diode, but without an estimate for the reverse saturation current density, the leakage current remained unknown, but appeared to dominate.

3. The UMKC diode exhibited large leakage currents ($\approx$10 $\mu$A estimated) at 5 V reverse bias. This exceeded the ideal by 4 orders of magnitude. C–V measurements indicated that the silicon was being depleted, but the depletion width did not extend beyond 25% of the silicon depth. The built-in voltage and dopant concentrations were calculated with the pre-characterization data, but the silicon dopant concentration computed was two orders of magnitude higher than expected. This may have contributed to high capacitance, which adversely affected the S/N ratio, and caused electric fields within the diode to be lower than ideal.

Recombination rates in the depletion region are improved with slow ion drift velocities. The weak electric fields were expected given the depletion width calculated from the C–V data. Pre-irradiation theoretical calculations suggested that the transient current collected from the n-type silicon side of the diode would exceed the measured steady state current, but only by a small margin.

The detector pulse-height spectrum presented no useable features, and although the oscilloscope trace activity increased in activity when the device was irradiated with a PuBe source, there was no change in the signal between the unshielded and cadmium-shielded spectra. Therefore, nothing observed in the oscilloscope could be attributed to ionization produced from the $^{10}$B(n, $\alpha$)$^{7}$Li reaction. Determining the root cause for this in the single pulse-height spectrum was the primary objective of device modeling. Experimental conclusions asserted that the detector response would not exceed the noise background given the weak electric fields in the depletion region. This argument was supported through modeling.

The UMKC diode was replicated in Davinci, and like the physical diode, simulation produced weak electric fields in the depletion region. This caused the charge collection times to become excessively long with respect to the fast timing characteristics expected of semiconductor detectors. The weak electric fields also led to higher recombination rates which depleted the charge carrier population. Ultimately, it was determined that the charge generated by a single $\alpha$ particle ionization track did not exceed the intrinsic noise charge of the preamplifier used for this experiment.

The effect of variations on other parameters, such as the silicon and boron carbide thickness, carrier concentrations, and ionizing particle paths, were analyzed. When the silicon thickness was reduced to 10 $\mu$m, the diode was over-depleted with only 5 V reverse bias and the electric field strength was constant throughout the diode. The charge induced with this geometry produced transient current pulses 1.75 times the reverse bias steady-state current. The conclusion drawn from the simulation study was that thinner silicon regions resulted in lower saturation voltages, which led to higher electric fields, improved charge carrier recombination escape probabilities, and thus enhanced the transient currents.

## 5.2 Recommendations for future work

The device modeling supported the conclusion that charge carriers were lost due to slow drift velocities, but this complication was resolved by reducing the silicon thickness so that the diode could be fully depleted. The motivation for this neutron detection study was to develop light-weight but efficient thermal neutron detectors that could be used in ports of entry to detect SNM smuggling attempts. Diodes such as the one modeled with only 10 $\mu$m would be worth investigating due to their inherently low saturation voltage. These diodes would likely require different fabrication techniques however due to the fragility of extremely thin silicon wafers.

Another option to explore would be the use of silicon wafers half the thickness of the ones used during this study. The simulation showed the depletion region depth extending past 250 $\mu$m at 5 V reverse bias. The detector would not then be operated in an over-depleted state, but it could possibly still collect an amount of charge that would exceed the intrinsic noise of the preamplifier. Recall also that the intrinsic noise level is often a function of capacitance. The capacitances of the UMKC diode was large, and the calculated silicon dopant concentration was greater than expected. Improving the fabrication techniques, even while still using silicon and boron carbide thicknesses identical to the diodes used in this study, may help reduce the diode capacitances and therefore the charge-sensitive preamplifier intrinsic noise charge.

The PECVD reactor at UMKC was recently disassembled and rebuilt to facilitate an improved and completely *in vacuo* diode fabrication process. The silicon wafers would be loaded into the the multi-chamber reactor, boron carbide and contacts would then be deposited (or sputtered) without exposing the devices to oxygen or other surface contaminants. Diodes produced via this procedure will likely have improved junctions, both at the p–n junction and the metal/semiconductor junctions where the contacts are sputtered. As material science technologies advance, it is highly likely

that true direct-conversion detectors could be produced. It is well worth the effort to test and analyze the improved diode electronic characteristics and any pulse-height spectra that could be obtained.

This experiment suffered from a dearth of useable diodes. It would be enlightening to acquire a set of samples, all created during the same deposition process, and compare the C–V characteristics. This would enable a comparison between the calculated dopant concentrations in order to determine whether the high dopant concentration calculated in this study was anomalous, or an indication of some other phenomena. The effective dopant concentration is of fundamental importance and it affects the depletion widths that could be obtained. It is thus a non-trivial matter and well-worth investigation.

Research focused on the trap densities and boron carbide/silicon interface defect densities and the corresponding effects on detector efficiencies may result in methodologies that profoundly improve the performance of these devices. There is little agreement between the electrical property values of boron carbide as reported by different literature sources. The modeling effort in this study could easily be augmented and improved with corrected boron carbide parameters. Many questions were left unanswered by the simulations including the topic of the charge collection length in partially-depleted detectors, and the effects of trapping. Resolving these matters may help in adding fidelity and address the literature differences concerning boron carbide and its electrical properties.

# Appendix A. Equipment and Settings

| List of Electronic Components | | | |
|---|---|---|---|
| Component | Manufacturer | Model | Serial |
| Pulser | Ortec | 480 | 2391 |
| Preamplifier | Ortec | 142IH | 2035 |
| Linear Amplifier | Ortec | 572A | 536 |
| ADCAM (MCB) | Ortec | 926 | 06165185 |
| Oscilloscope | Tektronics | DP07104 | B022189 |
| Bias Supply | Ortec | 478 | 41975 |

| Summary of Component Settings | | | |
|---|---|---|---|
| Component | Parameter | Diode Device | Resistive Device |
| Linear Amplifier | Shaping Time | 2 $\mu$s | 2 $\mu$s |
| | Coarse Gain | 500 | 50 |
| | Fine Gain | 5.0 | 5.65 |
| ADCAM (MCB) | LLD | 0.576 V | 0.08 V |
| | Conversion Gain | 512 | 1024 |
| Bias Supply | | 40 V | 1000 V |

# Appendix B. Calculations

## B.1 Diode Parameter Calculation

### B.1.1 UMKC Built-in Voltage

$1/C^2$, given the linear dependence of ($V_{bi}$ – V), was used to calculate $V_{bi}$.
Line of Fit: $y = 6.929\times10^{17} - 2.905\times10^{18}V$

$$\left(\frac{1}{C}\right)^2 = \left(\frac{2\left(\epsilon_{si}N_D + \epsilon_{bc}N_A\right)\left(V_{bi} - V\right)}{q\epsilon_{si}\epsilon_{bc}N_DN_A}\right)$$

when $V_{bi} = V$

$$\left(\frac{1}{C}\right)^2 = 0$$

$$0 = m\left(V - V_{bi}\right) + b$$

$$V_{bi} = \boxed{0.239\ [\mathrm{V}]}$$

$N_D$ and $N_A$ could then be determined. Mathematica "FindFit" command was used to accomplish this.

$N_D(si) \rightarrow \boxed{3.13\times10^{13}[\mathrm{cm}^{-3}]}$ $N_A(bc) \rightarrow \boxed{7.0\times10^{12}[\mathrm{cm}^{-3}]}$

The constants used for the calculations above are given below.

$q = 1.602\times10^{-19}$
$m = -2.905\times10^{18}$
$b = 6.929\times10^{17}$
$k = 11.9$
$\epsilon_0 = 8.85418\times10^{-14}$
$\epsilon_s = k\epsilon_0$
$\epsilon_{BC} = 8\epsilon_0$

The UNL diode did not have $1/C^2$ linearity; the dopant concentrations and built in voltage could not be calculated, but the capacitance data could be used to approximate the depletion width (shown below).

### B.1.2 UMKC and UNL diode hetero-junction calculations

$$C_j = \left( \frac{\epsilon_n}{x_n} + \frac{\epsilon_p}{x_p} \right)^{-1}$$
$$W = \epsilon_n \left( \frac{x_p}{\epsilon_p} + \frac{1}{C_j} \right) + x_p$$

| | UMKC | UNL |
|---|---|---|
| $x_p$ [$\mu$m] | 1.5 | 2.0 |
| Depletion width approximation | | |
| $W(V=0)$ | 10.94 | 136.1 |
| $W(V-5)$ | 44.53 | 128.8 |

## B.2 Pulse Prediction Calculations

The constants used to calculate charge collection times ($t_c$), transient currents ($I_{transient}$), and time constant ($\tau$) are given below.
$E_{dep} = 1.77 \times 10^6$ [eV]
$q = 1.602 \times 10^{-19}$ [C]
$E_{pr} = 3.62$ [eV]
$t_{plasma} = 5 \times 10^{-9}$ [s]
$W = 44.5261 \times 10^{-4}$ [cm] (UMKC diode depletion width at 5 V)
$\mu_{Si} = 1400$ [cm$^2$/V–s]
$\mu_{BC} = 0.00075$ [cm$^2$/V–s]

**Charge collection time**

$$t_c = \frac{d}{\mathcal{E}\mu}$$
$$\mathcal{E}(x) = \frac{qN_D}{\epsilon}(W - x)$$
$$t_c(x) = \frac{\epsilon}{q\mu N_D} \log \frac{W}{W - x_0}$$

$t_c$ Si [s] $\rightarrow \boxed{2.83\times10^{-9}\ [s]}$ $t_c$ BC [s]$\rightarrow \boxed{1.78\times10^{-4}\ [s]}$

Charge collection times can differ by 5 orders of magnitude. Only the charge collected within the instrumental circuit time constant will be integrated on the preamplifier capacitor.

**Time constant**

$$\tau = RC$$
$$C = \left[\frac{1}{C1} + \frac{1}{C2}\right]^{-1}$$

$R = 93\ [\Omega]$ (reported by [42])
$C1 = 10000\times10^{-12}$ [F] (reported by [42])
$C2 = 0.05\times10^{-9}$ [F] (measured)
Time Constant, $\tau \rightarrow \boxed{4.63\times10^{-9}\ [s]}$

**Transient current calculation**

$$I_{\text{transient}} = 2\frac{E_{dep}q}{E_{pr}\left(t_c + t_{plasma}\right)}$$

$I_{trans}$(Si)$\rightarrow \boxed{2.00\times10^{-5}\ [A]}$ $I_{trans}$(BC)$\rightarrow \boxed{8.79\times10^{-10}\ [A]}$

The transient current for the Silicon side is on the same order of magnitude as the leakage current (estimated 10 $\mu$A) at the 5 V reverse bias. The transient current on the BC side is 5 orders of magnitude less than the leakage current. Only current collected from the n-type silicon side has chance of being observed.

**Diffusion Length calculation**

$L_p = \sqrt{D_p\tau_p}$
$\tau_p = \frac{m_n}{q}$
$D_p = \left(\frac{kT}{q}\right)\mu_p$
$k = 1.38\times10^{-23}$ [J/K]
$T = 300$ [K]

Carrier Lifetime $\rightarrow \boxed{1.8\times10^{-9}\ [s]}$ Diffusion Constant $\rightarrow \boxed{11.6\ [cm^2/s]}$

Diffusion Length → $\boxed{1.4\ [\mu\text{m}]}$

**Saturation Current**

$q = 1.602\times10^{-19}$ [C]
$N_C = 10^{19}$ [cm$^{-3}$]
$N_V = 10^{19}$ [cm$^{-3}$]
$E_g = 0.9$ [eV]
$k = 8.6174\times10^{-5}$ [eV/K]
$T = 300$ [K]
$V_{th} = \frac{kT}{q}$ [V]

Silicon
$\mu_e = 1350$ [cm$^2$/V–s]
$\mu_h = 450$ [cm$^2$/V–s]
Boron Carbide
$\mu_e = .001$ [cm$^2$/V–s]
$\mu_h = .00075$ [cm$^2$/V–s]

$N_A$ and $N_B$ were calculated from C–V data.
$N_A = 7.0\times10^{12}$ [cm$^{-3}$] — effective dopant concentration in boron carbide
$N_D = 3.13\times10^{12}$ [cm$^{-3}$] — impurity concentration in silicon
$m_1 = 0.69\ m_0$ [kg] — mass of holes in silicon
$m_2 = 5\ m_0$ [kg] — mass of electrons in boron carbide
$m_0 = 0.91\times10^{-30}$ [kg] — mass of electron

$$n_i = \sqrt{N_C N_V}\exp\left[-\frac{E_g}{2V_{th}}\right]$$

$n_i$(silicon) → $\boxed{9.65\times10^{9}\ [\text{cm}^{-3}]}$ $n_i$(BC) → $\boxed{2.75761\times10^{11}\ [\text{cm}^{-3}]}$

$$D_{n,p} = \frac{kT}{q}\mu_{n,p}$$
$$\tau_{p,n} = \frac{\mu_{n,p} m_{2,1}}{q}$$
$$L_{n,p} = \sqrt{D_{n,p}\tau_{n,p}}$$

$$
\begin{aligned}
J_s &= J_n(\text{Boron Carbide}) + J_p(\text{Silicon}) \\
&= \frac{D_n n_i^2 q}{L_n N_A} + \frac{D_p n_i^2 q}{L_p N_D} \\
&= \boxed{5.3\times10^{-5}\ [\text{A/cm}^2]}
\end{aligned}
$$

### B.3 Neutron Emission Rate

This calculation was originally performed by [45] and has been modified according to [43] to accurately predict to the neutron emission rate at the time of the experiment.
NAv= $6.022\times10^{23}$

$t_1$=24110
$t_2$=6564
$t_3$=14.35
$t_4$=432.2

$\text{Mass}_{\text{Tot}}$=76.36
$W_1$=.9102
$W_2$=0.08098
$W_3$=0.00844

$\text{Mass}_1$=$\text{Mass}_{\text{Tot}}$ $W_1$
$\text{Mass}_2$=$\text{Mass}_{\text{Tot}}$ $W_2$
$\text{Mass}_3$=$\text{Mass}_{\text{Tot}}$ $W_3$

Atomic Masses
$\text{AM}_1$=239.052156
$\text{AM}_2$=240.053808
$\text{AM}_3$=241.0568453

$$
\begin{aligned}
N_{\text{i=1:3}} &= \frac{\text{Mass}_i}{\text{AM}_i}\text{NAv} \\
\lambda_{i=1:4} &= \frac{\text{Log[2]}}{t_{\frac{1}{2}i}}
\end{aligned}
$$

DateDifference[{1961,3,23},{1965,5,17},"Year"]
Time elapsed = 4.15068, Years

This time will be used to calculate $\mathcal{A}_0$ within the exponential terms.

$$\begin{aligned}
\mathcal{A}_1 &= 9.86\times10^6 \\
\mathcal{A}_0 &= \frac{\mathcal{A}_1}{\left(1+1.23\left(\frac{\lambda_4\lambda_3 \mathrm{N3}}{(\lambda_1 \mathrm{N1}+\lambda_2 \mathrm{N2})(\lambda_3-\lambda_4)}\left(\mathrm{Exp}\left[-4.151\lambda_4\right]-\mathrm{Exp}\left[-4.15\lambda_3\right]\right)\right)\right)} \\
\mathcal{A}[t] &= \mathcal{A}_0\left(1+1.23\left(\frac{\lambda_4\lambda_3 \mathrm{N3}}{(\lambda_1 \mathrm{N1}+\lambda_2 \mathrm{N2})(\lambda_3-\lambda_4)}\left(\mathrm{Exp}\left[-\lambda_4 t\right]-\mathrm{Exp}\left[-\lambda_3 t\right]\right)\right)\right)
\end{aligned}$$

$\mathcal{A}[0]$=9.31466×10$^6$
DateDifference[{1961,3,23},{2011,12,8},"Year"]
Time elapsed = 50.7104, Years
$\mathcal{A}[50.7] \rightarrow \boxed{1.19182\times10^7\ [\mathrm{s}^{-1}]}$

### B.3.1 Reaction Rate Density

$\mathcal{A}$=1.19182×10$^7$[$s^{-1}$]
$\rho$=2.55 [g/cm$^3$] density of boron carbide [36]
$m_a$=78.161 [g/mol] atomic mass of boron carbide ($B_5CH_{12}$)
$N_{AV}$=6.022×10$^{23}$ [atoms/mol]
$\sigma_{th}$=3880×10$^{-24}$ [cm$^2$]
$r$=0.252 [cm] diode radius (assuming spherical geometry due to isotropic source emission)
$d$=20.32 [cm] distance between detector and source
$\mathcal{B}$=.94 branching ratio of the reaction

$$\begin{aligned}
RRD &= \Sigma\Phi_{th} \\
\Phi_{th} &= \frac{\mathcal{A}\mathcal{B}\Omega}{4\pi} \\
\Omega &= 2\pi\left[1-\frac{\sqrt{r^2+d^2}}{d}\right] \\
\Sigma &= \sigma_{th}N \\
N &= \rho m_a N_{AV}
\end{aligned}$$

Thermal Flux, $\Phi_{th} \rightarrow \boxed{464\ [\mathrm{n/cm^2 s}]}$
Macroscopic Cross Section, $\Sigma \rightarrow \boxed{24578\ [\mathrm{cm^{-1}}]}$
Rate Reaction Density, $RRD \rightarrow \boxed{1.14\times10^7\ [\mathrm{cm^{-3}s^{-1}}]}$

# Appendix C. Davinci Input

```
TITLE Diode 2 Simple Diode

MESH DIAG.FL
X.MESH X.MIN=0 X.MAX=30.0 H1=0.2 H2=10. H3=0.2 SUMMARY
X.MESH X.MIN=30 X.MAX=250.0 H1=10. H2=100 H3=10. SUMMARY

Y.MESH Y.MIN=0. Y.MAX=10.0 H1=0.1 H2=.5 H3=0.1 SUMMARY
Y.MESH Y.MIN=10.0 Y.MAX=500 H1=0.5 H2=100 H3=.5 SUMMARY

Z.MESH Z.MIN=0 Z.MAX=30 H1=0.2 H2=10 H3=0.2 SUMMARY
Z.MESH Z.MIN=30 Z.MAX=250 H1=10 H2=100 H3=10 SUMMARY

$Defining the region materials and electrodes
REGION NAME=NREG X.MAX=250. Y.MIN=1.0 Y.MAX=500 Z.MAX=250. SIL-
ICON
REGION NAME=PREG X.MAX=250 Y.MAX=1.0 Z.MAX=250 SEMICOND
ELECTR NAME=PCON TOP
ELECTR NAME=NCON BOTTOM

PROFILE REGION=NREG UNIFORM N-TYPE N.PEAK=1e11
PROFILE REGION=PREG UNIFORM P-TYPE N.PEAK=4.2e13

MATERIAL TAUN0=1E-7 TAUP0=1E-6 SILICON
$MOBILITY SILICON MUN0=0.001
$MOBILITY SILICON MUP0=0.00075

MATERIAL SEMICOND EG.MODEL=3 EG300=0.9 TAUN0=1e-8 TAUP0=1e-8
PERMITTI=8
+ AFFINITY=4.58 NC300=1E19 NV300=1E19
SAVE MESHFILE OUT.FILE=DIODE2B.tdr tdr
MODELS SRH AUGER FLDMOB BGN CCSMOB

$CONTACT NAME=NCON RESIST=4.0E3 CAPAC=0.25E-13 PRINT

SYMBOL NEWTON CARRIERS=2
SOLVE INIT
METHOD ITLIMIT=10

PLOT.3D BOX GRID FILL TITLE="PHOTODIODE GRID REGRID" SCALE
CAMERA=(-500,-500,-500)

SOLVE V(NCON)=0 ELECTRODE=NCON VSTEP=1 NSTEP=5
```

PLOT.1D E.FIELD X.START=0 X.END=0 Y.START=0 Y.END=500 Z.START=0
Z.END=0 TITLE="ELEC FIEL" OUT.FILE=EFLD5V.dat

PHOTOGEN DCHR =0.2 T0=3.0E-12 TC=1.9E-12 LETFILE=dve182let PC.UNITS
$+ X.START=250.0 X.END=250.0 Y.MIN=1. Y.MAX=10.
$+ Z.START=250. Z.END=250.
SOLVE TSTEP=0.5E-12 TSTOP=1.0E-10 OUT.FILE=alpha5Va

PLOT.1D X.AXIS=TIME Y.AXIS=I(NCON) BOTTOM=-2E-3
+ COLOR=2 POINTS TITLE="Example 4 - Current vs. Time" OUT.File=diode2BNPULSE.dat
EXIT

# Bibliography


[1] Nuclear Regulatory Commission, "Special Nuclear Material," accessed January, 2012. [Online]. Available: http://www.nrc.gov/materials/sp-nucmaterials.html

[2] J. Shultis and R. Faw, "Radiation shielding," La Grange Park, IL American Nuclear Society, Inc, 2000, as reported by Bevins, J., "Characterization of a boron carbide hetero-junction neutron detector", AFIT Thesis, 2011.

[3] National Nuclear Data Center, "Nuclear structure and decay data, NUDAT 2.6," 2012, accessed January, 2012. [Online]. Available: http://www.nndc.bnl.gov/nudat2

[4] R. Kouzes, E. Siciliano, J. Ely, P. Keller, and R. McConn, "Passive neutron detection at borders," in *Nuclear Science Symposium Conference Record, 2007. NSS '07. IEEE*, vol. 2, no. 24-4, Nov 2007, pp. 1115 –1119.

[5] A. N. Caruso, "The physics of solid-state neutron detector materials and geometries," *Journal of Physics: Condensed Matter*, vol. 22, no. 44, p. 443201, 2010.

[6] National Nuclear Data Center, "Evaluated nuclear data file (ENDF/B-VII.0) retrieval and plotting," 2006, accessed on November 24, 2011. [Online]. Available: http://www.nndc.bnl.gov/sigma/

[7] National Institute of Standards and Technology, "XCOM: Photon Cross Sections Database (NIST Standard Reference Database 8)," 2010, accessed on November 24, 2011. [Online]. Available: http://www.nist.gov/pml/data/xcom/index.cfm

[8] S.-D. Hwang, D. Byun, N. J. Ianno, P. A. Dowben, and H. R. Kim, "Fabrication of boron-carbide/boron heterojunction devices," *Applied Physics Letters*, vol. 68, no. 11, pp. 1495–1497, March 1996.

[9] C. Lundstedt, A. Harken, E. Day, B. W. Robertson, and S. Adenwalla, "Modeling solid-state boron carbide low energy neutron detectors," *Nuclear Instruments and Methods in Physics Research Section A: Accelerators, Spectrometers, Detectors and Associated Equipment*, vol. 562, no. 1, p. 380, 2006.

[10] B. W. Robertson, S. Adenwalla, A. Harken, P. Welsch, J. I. Brand, P. A. Dowben, and J. P. Claassen, "A class of boron-rich solid-state neutron detectors," *Applied Physics Letters*, vol. 80, no. 19, pp. 3644–3646, 2002.

[11] D. S. McGregor, S. M. Vernon, H. K. Gersch, and D. K. Wehe, "Self-biased boron-10 coated high purity epitaxial gaas neutron detectors," *IEEE Transactions on Nuclear Science*, vol. 1, no. 4, pp. 1364–1370, 2000.

[12] D. S. McGregor and J. K. Shultis, "Spectral identification of thin-film-coated and solid-form semiconductor neutron detectors," *Nuclear Instruments and Methods in Physics Research Section A: Accelerators, Spectrometers, Detectors and Associated Equipment*, vol. 517, no. 1-3, p. 180, 2004.

[13] A. D. Harken, E. E. Day, B. W. Robertson, and S. Adenwalla, "Boron-rich semiconducting boron carbide neutron detector," *Japanese Journal of Applied Physics*, vol. 44, no. 1A, pp. 444–445, 2005.

[14] G. F. Knoll, *Radiation detection and measurement*, 4th ed. Hoboken, NJ: John Wiley and Sons, 2010.

[15] S. M. Sze, *Semiconductor devices, physics and technology*, 2nd ed. Hoboken, NJ: John Wiley and Sons, Inc., 2002.

[16] H. Spieler, *Semiconductor detector systems*, ser. Series on semiconductor science and technology. Oxford University Press, 2005.

[17] N. Hong, J. Mullins, K. Foreman, and S. Adenwalla, "Boron carbide based solid state neutron detectors: the effects of bias and time constant on detection efficiency," *Journal of Physics D: Applied Physics*, vol. 43, no. 27, p. 275101, 2010.

[18] H. Werheit, "Present knowledge of electronic properties and charge transport of icosahedral boron-rich solids," *Journal of Physics: Conference Series*, vol. 176, no. 1, p. 012019, 2009.

[19] R. Schmechel and H. Werheit, "On the dynamical conductivity in icosahedral boron-rich solids," *Journal of Physics: Condensed Matter*, vol. 8, no. 39, p. 7263, 1996.

[20] H. Werheit, "Are there bipolarons in icosahedral boron-rich solids?" *Journal of Physics: condensed Matter*, vol. 19, no. 18, p. 186207, 2007.

[21] R. Schmechel and H. Werheit, "Evidence of the superposition of drude type and hopping type transport in boron-rich solids," *Journal of Solid State Chemistry*, vol. 133, no. 1, pp. 335–341, 10 1997.

[22] H. Werheit, R. Schmechel, K. Kimura, R. Tamura, and T. Lundstrm, "Evidence of the relationship of the electronic properties of icosahedral boron-rich solids and icosahedral quasicrystals," *Journal of Solid State Chemistry*, vol. 133, no. 1, pp. 160–163, 10 1997.

[23] H. Werheit, "On excitons and other gap states in boron carbide," *Journal of Physics: Condensed Matter*, vol. 18, no. 47, p. 10655, 2006.

[24] K. Kimura, A. Hori, M. Takeda, H. Yamashita, and H. Ino, "Possibility of semiconducting quasicrystal in boron-rich solids," *Journal of Non-Crystalline Solids*,

vol. 153-154, no. 0, p. 398, 1993, proceddings of the Fourth International Conference on Quasicrystals.

[25] S. Adenwalla, P. Welsch, A. Harken, J. I. Brand, A. Sezer, and B. W. Robertson, "Boron carbide/n-silicon carbide heterojunction diodes," *Applied Physics Letters*, vol. 79, no. 26, pp. 4357–4359, 2001. [Online]. Available: http://link.aip.org/link/?APL/79/4357/1

[26] A. V. Okotrub, L. G. Bulusheva, and V. V. Volkov, "Electron interactions in the closo-carboranes 1,2- and 1,7-$C_2B_{10}H_{12}$," *Journal of Molecular Structure*, vol. 520, no. 1-3, pp. 33–38, 2000.

[27] A. N. Caruso, R. B. Billa, S. Balaz, J. I. Brand, and P. A. Dowben, "The heteroisomeric diode," *Journal of Physics: Condensed Matter*, vol. 16, no. 10, p. 139, 2004.

[28] A. Caruso, "High efficiency fast and slow neutron detection by solid state heterostructures," 2010, presentation to Air Force Institute of Technology, Wright-Patterson AFB, OH, May 2010, as reported by Bevins, J., "Characterization of a boron carbide hetero-junction neutron detector", AFIT Thesis, 2011.

[29] A. N. Caruso, P. A. Dowben, S. Balkir, N. Schemm, K. Osberg, R. W. Fairchild, O. B. Flores, S. Balaz, A. D. Harken, B. W. Robertson, and J. I. Brand, "The all boron carbide diode neutron detector: Comparison with theory," *Materials Science and Engineering: B*, vol. 135, no. 2, p. 129, 2006.

[30] C. Wood and D. Emin, "Conduction mechanism in boron carbide," *Phys.Rev.B*, vol. 29, no. 8, pp. 4582–4587, Apr 1984.

[31] S. Lee, J. Mazurowski, G. Ramseyer, and P. A. Dowben, "Characterization of boron carbide thin films fabricated by plasma enhanced chemical vapor deposition from boranes," *Journal of Applied Physics*, vol. 72, no. 10, pp. 4925–4933, 1992.

[32] P. A. Dowben and S. Lee, "The properties of boron carbide/silicon heterojunction diodes fabricated by plasma-enhanced chemical vapor deposition," *Applied Physics A: Materials Science and Processing*, vol. 58, no. 3, pp. 223–227, 1994.

[33] E. Day, M. J. Diaz, and S. Adenwalla, "Effect of bias on neutron detection in thin semiconducting boron carbide films," *Journal of Physics D: Applied Physics*, vol. 39, no. 14, p. 2920, 2006. [Online]. Available: http://stacks.iop.org/0022-3727/39/i=14/a=007

[34] M. M. Paquette, W. Li, M. S. Driver, S. Karki, A. N. Caruso, and N. A. Oyler, "The local physical structure of amorphous hydrogenated boron carbide: insights from magic angle spinning solid-state nmr spectroscopy," *Journal of Physics: Condensed Matter*, vol. 23, no. 43, p. 435002, 2011.

[35] Y. B. Losovyj, D. Wooten, J. C. Santana, J. M. An, K. D. Belashchenko, N. Lozova, J. Petrosky, A. Sokolov, J. Tang, W. Wang, N. Arulsamy, and P. A. Dowben, "Comparison of n-type $Gd_2O_3$ and Gd-doped $HfO_2$," *Journal of Physics: Condensed Matter*, vol. 21, no. 4, p. 045602, 2009.

[36] J. Bevins, "Characterization of a boron carbide hetero-junction neutron detector," MS thesis, AFIT/GNE/ENP/11-M02, Department of Engineering Physics, Air Force Institute of Technology(AU), Wright-Patterson AFB, OH, 2011.

[37] S. Sze and K. Ng, *Physics of semiconductor devices*, 3rd ed., ser. Wiley-Interscience publication. Hoboken, NJ: Wiley-Interscience, 2007.

[38] O. Breitenstein, "Understanding shunting mechanisms in silicon cells: A review," accessed February 25, 2012. [Online]. Available: http://www.mpi-halle.mpg.de/mpi/publi/pdf/7497_07.pdf

[39] B. Zeghbroeck, "Principles of semiconductor devices," 2007. [Online]. Available: http://ecee.colorado.edu/~bart/book/book/index.html

[40] N. Hong, M. A. Langell, J. Liu, O. Kizilkaya, and S. Adenwalla, "Ni doping of semiconducting boron carbide," *Journal of Applied Physics*, vol. 107, no. 2, 2010.

[41] J. Petrosky, Professor, Department of Engineering Physics, Air Force Institute of Technology, Personal Correspondence, 02 March 2012.

[42] Ortec, "142IH Preamplifier Datasheet," access January 2012. [Online]. Available: www.ortec-online.com/download/142IH.pdf

[43] Nuclear Materials and Equipment Corporation, "Plutonium Beryllium Source datasheet, SN: 800I28," Apollo, Pa, 1965, datasheet on hand at The Ohio State Nuclear Reactor Lab, Columbus, OH. Source was used on 01 and 08 December 2011.

[44] C. Young, "Gadolinium oxide/silicon thin film heterojunction solid-state neutron detector," MS thesis, AFIT/GNE/ENP/10M-10, Department of Engineering Physics, Air Force Institute of Technology(AU), Wright-Patterson AFB, OH, 2010.

[45] D. Blasy, "Neutron detection utilizing gadolinium doped hafnium oxide films," MS thesis, AFIT/GNE/ENP/08-M02, Department of Engineering Physics, Air Force Institute of Technology, Wright-Patterson AFB, OH, 2008.

[46] L. Stewart, "Neutron spectrum and absolute yield of a plutonium-beryllium source," *Phys. Rev.*, vol. 98, pp. 740–743, May 1955.

[47] A. Bickley, "Design optimization of a layered boron based solid state neutron detector," in IEEE Nuclear Science Symposium Conference Proceedings, November 2011.

[48] D. S. McGregor, "Reporting detection efficiency for semiconductor neutron detectors: A need for a standard," *Nuclear Instruments and Methods in Physics Research Section A: Accelerators, Spectrometers, Detectors and Associated Equipment*, vol. 632, no. 1, pp. 167 – 174, 2011.

[49] Z. Li, V. Eremin, N. Strokan, and E. Verbitskaya, "Investigation of the type inversion phenomena: resistivity and carrier mobility in the space charge region and electrical neutral bulk in neutron irradiated silicon $p^+$-n junction detectors," *IEEE Transactions on Nuclear Science*, vol. 40, no. 4, pp. 367–375, aug 1993.

[50] M. Takada, T. Nunomiya, T. Ishikura, and T. Nakamura, "Charge-collection length induced by proton and alpha particle injected into silicon detectors due to funneling effect," *Nuclear Science, IEEE Transactions on*, vol. 56, no. 1, pp. 337–345, feb. 2009.

[51] National Institute of Standards and Technology, "Alpha stopping power and ranges, (ASTAR)," 2012, accessed January, 2012. [Online]. Available: http://physics.nist.gov/PhysRefData/Star/Text/ref.html

[52] "Taurus Medici Davinci User Guide," Version Y–2006.06, Synopsys Inc., 2006.

[53] S. McHale, "The effects of rare earth doping on gallium nitride thin films," Dissertation, AFIT/DS/ENP/11-S05, Department of Engineering Physics, Air Force Institute of Technology, Wright-Patterson AFB, OH, 2011.

# REPORT DOCUMENTATION PAGE

*Form Approved*
*OMB No. 0704–0188*



| 1. REPORT DATE *(DD–MM–YYYY)* | 2. REPORT TYPE | 3. DATES COVERED *(From — To)* |
|---|---|---|
| 22–03–2012 | Master's Thesis | Aug 2011 — Mar 2012 |

**4. TITLE AND SUBTITLE**

Neutron Detection using Amorphous Boron-Carbide Hetero-Junction Diodes

**5a. CONTRACT NUMBER**

**5b. GRANT NUMBER**

**5c. PROGRAM ELEMENT NUMBER**

**6. AUTHOR(S)**

Thomas P. McQuary, MAJ, USA

**5d. PROJECT NUMBER**

AFIT/NUCL/ENP/12-M06

**5e. TASK NUMBER**

**5f. WORK UNIT NUMBER**

**7. PERFORMING ORGANIZATION NAME(S) AND ADDRESS(ES)**

Air Force Institute of Technology
Graduate School of Engineering and Management (AFIT/EN)
2950 Hobson Way
WPAFB OH 45433-7765

**8. PERFORMING ORGANIZATION REPORT NUMBER**

AFIT/NUCL/ENP/12-M06

**9. SPONSORING / MONITORING AGENCY NAME(S) AND ADDRESS(ES)**

DTRA/OP-ONIU (COL Scott Horton)
1680 Texas ST. SE
Kirtland AFB, NM 87117-5776
(506) 846-8746, scott.horton@dtra.mil

**10. SPONSOR/MONITOR'S ACRONYM(S)**

DTRA/OP-ONIU

**11. SPONSOR/MONITOR'S REPORT NUMBER(S)**

**12. DISTRIBUTION / AVAILABILITY STATEMENT**

APPROVED FOR PUBLIC RELEASE: DISTRIBUTION UNLIMITED.

**13. SUPPLEMENTARY NOTES**

**14. ABSTRACT**

The high energy products of the $^{10}B(n,\alpha)^{7}Li$ neutron capture reaction were explored as a means of thermal neutron detection in thin film amorphous boron carbide (a—$B_5C$:$H_x$) on n-type silicon hetero-junction diodes. Pulse height spectroscopy was conducted on the diodes while they were subjected to a moderated plutonium-beryllium (PuBe) source. Neutron capture could not be confirmed experimentally in any of the devices tested. Device modeling was performed to investigate the cause for the diode detector's negative response. A 1.47 MeV $\alpha$ particle produced transient current of $10^{-7}$ A and the induced was 4.7 times less than intrinsic noise charge of the preamplifier. Further investigation of the model emphasized the transient current magnitude was most dependent on the electric field strength. The possibility of direct-conversion hetero-junction neutron detectors was not experimentally confirmed, but simulations using only 10$\mu$m of silicon however did generate transient currents 2 factors larger than steady-state reverse bias currents.

**15. SUBJECT TERMS**

Neutron detection, Amorphous Boron Carbide, Solid-State detectors, Taurus Davinci Device Modeling

| 16. SECURITY CLASSIFICATION OF: | | | 17. LIMITATION OF ABSTRACT | 18. NUMBER OF PAGES | 19a. NAME OF RESPONSIBLE PERSON |
|---|---|---|---|---|---|
| a. REPORT | b. ABSTRACT | c. THIS PAGE | | | LTC John W. McClory |
| U | U | U | U | 107 | 19b. TELEPHONE NUMBER *(include area code)* (937) 255-3636, x7308; john.mcclory@afit.edu |